A novel shared mechanism for Bacteroidota protein transport and gliding motility

Authors:

Xiaolong Liu[1]*, Marieta Avramova[1], Justin C. Deme[2], Rachel L. Jones[1], Camilla A.K. Lundgren[1], Susan M. Lea[2]*, and Ben C. Berks[1]*

Affiliations:

[1] Department of Biochemistry, University of Oxford, Oxford, United Kingdom.

[2] Center for Structural Biology, Center for Cancer Research, National Cancer Institute, Frederick, Maryland, United States of America.

* Corresponding authors. Email ben.berks@bioch.ox.ac.uk, susan.lea@nih.gov, xiaolong.liu@bioch.ox.ac.uk

Abstract

Bacteria of the phylum Bacteroidota are major human commensals and pathogens in addition to being abundant members of the wider biosphere. Bacteroidota move by gliding and they export proteins using the Type 9 Secretion System (T9SS). Here we discover that gliding motility and the T9SS share a novel mechanism of energisation in which outer membrane proteins are covalently attached by disulfide bonds to a moving internal track structure which propels them through the membrane. We determined the structure of a representative Bacteriodota mobile track by obtaining the cryoEM structure of a 3 MDa circular mini-track from *Porphyromonas gingivalis*. Our discoveries identify a novel mechanistic and evolutionary link between gliding motility and T9SS-dependent protein transport.

Introduction

The Bacteroidota (formerly Bacteroidetes) are one of the three main phyla of Gram-negative bacteria. They are the most abundant Gram-negative commensals in the human gut and are also major components of other human microbiota[1]. The phylum includes major human opportunistic anaerobic pathogens responsible for sepsis as well as oral pathogens such as *Porphyromonas gingivalis* which cause severe dental disease (periodontitis). More broadly, the Bacteriodota are widely distributed in environments throughout the biosphere[2]. Two key distinctive features of the Bacteroidota are the ability to move using gliding motility and to export proteins using the Type 9 Secretion System (T9SS).

The T9SS transports substrate proteins across the outer membrane (OM) and plays critical roles in Bacteroidota virulence and nutrition[3-9]. During Type 9 transport the substrate protein moves through a channel in the OM translocon protein SprA to form a complex with a docked OM `carrier protein'[10](**Fig. 1a**). The resulting substrate-carrier protein complex is then ejected from the translocon using an energetic input from a multi-protein Power Chain[11]. T9SS substrates fall into two classes[12]. Type A substrates are extracted from the translocon by the general carrier protein PorV and are subsequently either released into the extracellular environment or covalently attached to cell surface lipopolysaccharide[11,13]. By contrast, Type B substrates each have their own dedicated carrier protein to which they remain bound thereby anchoring them to the cell surface[14,15].

Gliding is the only mode of motility present in the Bacteroidota and allows rapid movement across solid surfaces[7,16]. It is present in most free-living Bacteroidota and some oral commensals and is mechanistically distinct from the gliding motility

exhibited by other phyla[16]. Bacteroidota gliding motility has been best studied in the soil bacterium *Flavobacterium johnsoniae*. Gliding in this organism is mediated by the cell surface adhesin SprB, which flows in helical trajectories up and down the cell[17-21]. When SprB adhesins attach to a solid surface the cell is propelled forward in a cork-screwing motion[10,19,21,22]. The SprB adhesin is anchored to the cell surface by the OM protein SprF [14,15,23](**Fig. 1a**). SprF is, in turn, thought to bind to a moving track structure at the inner face of the OM resulting in the propulsion of the attached adhesin along the cell body[19,24,25]. In current models of the gliding apparatus the track is predominantly or exclusively a polymer of the OM-anchored lipoprotein GldJ[19,24,26].

Bacteroidota gliding has long been known to depend on the organism possessing a T9SS in order to transport the gliding adhesins to the cell surface[27]. For example, in *F. johnsoniae* the adhesin SprB is a Type B T9SS substrate and SprF is its cognate carrier protein[14,15]. More recently it has shown that gliding motility and Type 9 transport are intimately mechanistically linked because they are both powered by the T9SS Power Chain[27-29]. In current models the Power Chain is composed of motor complexes that transduce the energy of the inner membrane protonmotive force into mechanical energy and transfer this across the periplasm to a Hub complex on the inner face of the OM[28,30,31](**Fig. 1a**). The Hub complex then distributes this mechanical energy both to the T9SS translocon and to the gliding machinery to power movement of the gliding track[28]. In the non-gliding pathogenic bacterium *Porphyromonas gingivalis* the Hub has been shown to be a megadalton ring-shaped molecule composed of many copies of the proteins PorK and PorN and anchored to the OM by the lipidated N-terminus of PorK[27,32-34]. In the gliding bacterium *F. johnsoniae* the PorKN-equivalent Hub proteins GldK and GldN[35] are assumed to form a similar ring structure, the outer rim of which

contacts the gliding track[16,26]. The motors are envisaged to rotate the Hub ring (`pinion') to drive the movement of the associated gliding track (`rack') [25,26].

Given the enormous mechanical forces exerted on the adhesins during gliding it would be anticipated that the adhesin carrier protein SprF forms an extremely strong interaction with the gliding track. However, we were unable to predict a plausible complex between SprF and the presumed track protein GldJ using AlphaFold3 (AF3) [36]. Intrigued by this observation we decided to investigate the nature of the interaction between SprF and the track. We uncovered an unanticipated and shared role for disulfide bonds in connecting gliding and T9SS components to moving internal track structures. This work leads to a radically new mechanistic model for the gliding motility apparatus and of its relationship to the T9SS.

Results

A twin-cysteine motif in the periplasmic tail of SprF is essential for gliding motility

In considering how the adhesin carrier protein SprF might interact with the gliding track we noticed that the periplasmic C-terminal tail of SprF contains a Cys-Xaa-Cys motif that is invariant in all close homologues (**Fig. 1b**). Since conserved cysteine residues often have a functional role, we examined whether this twin-cysteine motif is required for SprF to function in gliding motility. Substituting either or both of the cysteine residues abolished gliding (**Fig. 1c**). Thus, both cysteine residues are

97 essential for SprF function. Control experiments confirmed that the cysteine
98 substitutions do not affect the levels or stability of SprF (**Supplementary Data Fig. 1**).

99 SprF can be considered to carry out two mechanistically separable functions. First,
100 it acts as a carrier protein for the export and surface-anchoring of the SprB adhesin.
101 Second, it attaches to the periplasmic gliding tracks to allow movement of the attached
102 adhesin. We used protease accessibility experiments to test whether the twin-cysteine
103 motif is required for SprF to fulfil its carrier protein functions (**Fig. 1d**). In these
104 experiments a protease is added to the medium around the cells and digests any SprB
105 molecules present on the cell surface. However, if export of SprB is unable to take
106 place (for example in a Δ*sprF* background in **Fig. 1d**), the adhesin remains inside the
107 cell and is protected from digestion by the external protease. Using this approach, we
108 found substitution of the SprF cysteine residues either singly or in combination had no
109 effect on the surface localization of SprB (**Fig. 1d**). Thus, the twin-cysteine motif is not
110 required for the carrier protein function of SprF.

111 To determine whether the twin-cysteine motif is, instead, required for the interaction
112 of SprF with the gliding track we carried out live cell single molecule tracking
113 experiments (**Fig. 1e, Supplementary Video 1**). In this approach fluorophore-labelled
114 SprB adhesin molecules are tracked as a proxy for the behaviour of the SprF
115 molecules to which they are bound. In a wild-type SprF background a large proportion
116 of the SprB molecules move on sustained helical trajectories as previously
117 reported[18,20,21,28]. However, removing the cysteine pair in SprF almost completely
118 suppresses this continuous helical movement. Thus, the twin-cysteine motif is required
119 for SprF to make normal interactions with the gliding track. Although most of the SprB
120 molecules in the cysteine-substituted background were close to stationary, a minority
121 still exhibited short, apparently directed motions. 3D tracking confirmed that the

122 handedness of these short trajectories matched the exclusively left handed geometry
123 of the gliding tracks[18-20] showing that these trajectories still represent SprB molecules
124 moving on a track (**Extended Data Fig. 1**). The adhesins with these short trajectories
125 showed frequent stopping behaviour, often for extended periods of time (> 10
126 seconds). During these `stops' the molecules could be either immobile or slowly
127 diffusive, and the adhesin often resumed helical movement in a different direction from
128 the trajectory before the `stop'. Thus, SprF is still able to interact with the gliding tracks
129 in the absence of the twin-cysteine motif, but these residual interactions are sporadic,
130 short term, and prone to aberrant behaviour. Control experiments show that if SprB
131 export is blocked by the complete removal of SprF (Δ*sprF*) then the non-exported SprB
132 molecules in the periplasm exhibit rapid isotropic diffusion that is quite distinct from
133 the behaviours observed when the SprF cysteine residues are removed.

134

135 **SprF is disulfide-bonded to GldK**

136 Conserved cysteines residues in periplasmic proteins are often involved in forming
137 disulfide bonds. This prompted us to explore whether the twin-cysteine motif in SprF
138 was involved in forming a disulfide link to the gliding track. To do this we first trapped
139 the thiol/disulfide state of the cellular proteome by treating *F. johnsoniae* with the
140 membrane-permeable thiol-reactive reagent *N*-ethylmaleimide (NEM). NEM forms an
141 irreversible adduct with free thiol groups. The modified thiols are no longer able to
142 attack and break disulfide bonds and so the disulfide bonds present in the cell are
143 preserved.

144 Treatment of *F. johnsoniae* cells with NEM resulted in almost the entire SprF pool
145 being recovered in a high molecular mass adduct running larger than 100 kDa (**Fig.**

146 **2a**). Formation of this adduct was reversed by addition of the thiol-containing reagent
147 DTT, confirming that the two proteins were linked by a disulfide bond (**Fig. 2a**).
148 Formation of the adduct also required the presence of the twin-cysteine motif in SprF,
149 demonstrating the involvement of these residues in the disulfide linkage (**Fig. 2a**).

150 SprF anchors the gliding adhesin SprB to the cell surface. We found that SprB was
151 required for the formation of the SprF-containing disulfide adduct (**Fig. 2a**). The
152 disulfide adduct was also missing in a strain in which export of SprB was blocked by
153 deletion of the T9SS translocon (Δ*sprA* strain, **Fig. 2b**), though not by removal of a
154 T9SS carrier protein that is not involved in SprB export (Δ*porV* strain, **Fig. 2b**),
155 confirming that SprB must be exported and loaded onto SprF for disulfide bond
156 formation to occur. The stability of the SprF adduct does not depend on active
157 movement of the SprB-SprF complex since it is still detected after dissipation of the
158 protonmotive force that powers the gliding apparatus[18,28] (**Extended Data Fig. 2a**).

159 To identify the partner protein to which SprF is disulfide linked we took a candidate
160 approach informed by our current understanding of the organisation of the gliding
161 motility apparatus. In this model the periplasmic domain of SprF interacts with a gliding
162 track constructed from GldJ protomers (**Fig. 1a**). Based on this model the partner
163 protein to which SprF is disulfide-linked should be GldJ. Surprisingly, however, no
164 adduct equivalent to that identified with SprF antibodies was detected by
165 immunoblotting against GldJ (**Fig. 2a**). This rules out GldJ as the binding partner of
166 SprF. Upon broadening our screen to other gliding components, we found that the
167 lipoprotein GldK was partially recovered in a disulfide-linked adduct with the same
168 molecular mass as that formed by SprF (**Fig. 2a**). Crucially this adduct was no longer
169 formed when the twin-cysteine motif of SprF was removed showing that the SprF is
170 the interacting partner (**Fig. 2a**). Thus, the Hub component GldK is the partner protein

171 to which SprF is disulfide linked. Because SprF is in continuous movement along the
172 gliding track, the covalent link between SprF and GldK implies that GldK is a
173 component of the track rather than being located in a separate Hub complex as
174 envisaged in the current gliding model (**Fig. 1a**).

175 We next attempted to identify the cysteine residue(s) in GldK that are involved in
176 forming the disulfide linkage with SprF. Discounting the lipidated N-terminal cysteine,
177 GldK contains two cysteine residues (Cys285 and Cys343). These cysteine residues
178 are highly conserved across GldK homologues (Fig. 3a). Gliding motility is blocked
179 when Cys343, but not Cys285, is substituted providing presumptive evidence that it is
180 Cys343 that forms the disulfide linkage with SprF (**Fig. 3b**). This is confirmed by
181 biochemical analysis which shows that the SprF-GldK disulfide bond is still present in
182 a *gldK*^{C285S} background but missing in a *gldK*^{C343S} strain (**Fig. 3c**). Export of the SprB
183 adhesin still takes place when the disulfide-bond forming Cys343 of GldK is
184 substituted, albeit with lower efficiency than in the wild-type strain (**Fig. 3d**).
185 Nevertheless, as with the SprF twin-cysteine deletion strain, single particle tracking
186 measurements fail to detect SprB molecules following the sustained helical trajectories
187 typical of gliding adhesins in wild-type cells. Although there are rare examples of
188 adhesins exhibiting short helical trajectories, most adhesins are close to stationary
189 (there is also a background of rapidly isotropically moving particles due to the elevated
190 levels of non-exported SprB molecules in the periplasm of this strain)(**Fig. 3e,**
191 **Supplementary Video 2**). Thus, for those adhesins that have been successfully
192 exported, the effects of removing GldK Cys343 on their mobility are equivalent to those
193 of removing the SprF twin-cysteine motif. This is as expected if these two groups of
194 cysteine residues are partners in the same disulfide bond.

195

196 **The SprF twin-cysteine residues have non-identical roles**

197 We next investigated the individual contributions of the two SprF Cys residues to
198 disulfide bond formation with GldK. Removing Cys326, but not Cys324, prevented
199 formation of the adduct with GldK (**Fig. 2a**). This shows that it is Cys326 that forms
200 the disulfide bond to GldK (**Fig. 3f**). Although the SprF-GldK disulfide bond still forms
201 when Cys324 is removed, the bond is only formed by a minority of the SprF molecules
202 present. This contrasts with the situation with the wild-type protein where almost the
203 entire SprF pool is crosslinked to GldK (**Fig. 2a**). Thus, Cys324 enhances the
204 efficiency of formation of the inter-protein disulfide bond. Our interpretation of this
205 observation is that Cys324 forms an intramolecular disulfide bond with Cys326, and
206 that this bond is then attacked by a cysteine thiol on GldK to form the SprF-GldK
207 disulfide link (**Fig. 3f**). Consequently, when the intramolecular disulfide bond in SprF
208 is absent in the SprF Cys324Ala variant, formation of the disulfide bond between the
209 remaining SprF cysteine and Cys343 in GldK requires an adventitious oxidant and so
210 occurs with low efficiency.

211 It is notable that the SprF-GldK adduct is present even without NEM treatment of
212 the bacteria in cells expressing the SprF Cys324A variant (**Fig. 2a**). This suggests that
213 Cys324 is responsible for the instability of the SprF-GldK disulfide linkage in wild-type
214 cells, which it presumably attacks to reform the intramolecular Cys324-Cys326
215 disulfide bond on SprF (**Fig. 3f**) Because NEM treatment of wild-type cells stabilises
216 almost the entire SprF pool in disulfide linked adducts with GldK (**Fig. 2a**), we can infer
217 that under physiological steady state conditions Cys324 is present almost exclusively
218 in the thiol state (and thus derivatized by NEM) and so the Cys324-Cys326/Cys326-
219 GldK disulfide equilibrium is positioned heavily towards the Cys326-GldK side (**Fig.
220 3f**). This is intuitively reasonable because the vicinal thiols in SprF are separated by

221 only a single amino acid residue and so the disulfide bond between them will be highly
222 strained and unstable relative to the Cys326-GldK disulfide. We interpret the need for
223 NEM treatment in our experimental analysis of disulfide bonding patterns as reflecting
224 the fact that SprF and GldK will irreversibly separate once solubilized in SDS if their
225 disulfide linkage is broken. Consequently, even very low levels of attack on the
226 disulfide bond between SprF and GldK by SprF Cys324 will, over time, remove the
227 SprF-GldK adduct from the sample. By contrast, in the cellular context SprF and GldK
228 are kept adjacent allowing their disulfide bond to be reformed if it is cleaved by SprF
229 Cys324.

230 Both cysteine residues in the C-tail of SprF are essential for gliding (**Fig. 1c**). This
231 behaviour is readily explained for Cys326 because this residue is required to form the
232 disulfide bond with GldK. However, this disulfide bond is still formed when Cys324 is
233 absent, raising the question of why this residue is needed for the cell to move. It is
234 possible that the small proportion of SprF molecules that are crosslinked to GldK in
235 this background (**Fig. 2a**) is insufficient to sustain gliding. It is also possible that the
236 gliding mechanism requires the crosslink between Cys326 and GldK to be dynamically
237 reversible, but that this is no longer possible without Cys324 to attack the intra-protein
238 disulfide bond (**Fig. 3f**). In an attempt to gain insight into these possibilities we
239 examined the effect of the single SprF cysteine substitutions on the mobility of
240 fluorophore-labelled adhesins (**Fig. 1e**). As expected, removal of Cys326 phenocopies
241 the behaviour of other backgrounds (*sprF*^{C324A,C326A}, *gldK*^{C343S}) that cannot form the
242 SprF-GldK disulfide bond (**Figs. 1e and 3e**). By contrast, removal of Cys324 produces
243 a mix of behaviours in which some adhesins perform sustained helical movements
244 (like cells with wild-type SprF) whilst others only move helically for short periods at
245 best (as in strains that cannot disulfide bond to GldK)(**Fig. 1e**), consistent with the

246 observation that only a proportion of the SprF molecules are disulfide-bonded to the
247 gliding track in these cells (**Fig. 2a**). If, as we hypothesise, the SprF-GldK disulfide
248 links in this strain cannot readily be reversed, then the fact that some adhesins (those
249 we have interpreted as associating with SprF molecules that are disulfide-linked to
250 GldK) are able to sustain continuous helical movement for multiple circuits of the cell
251 implies that the ability to break the disulfide linkage is not a requirement for normal
252 adhesin motion. This conclusion is strengthened by the observation that the movement
253 of another protein that moves on the gliding track (SprC) [37] is unimpaired in the
254 *sprF*^{C324A} background (**Fig. 1e**). Thus, locking some SprF molecules to GldK does not
255 impede the movement of the track network. Since these experiments do not detect
256 defects in adhesin mobility upon removal of SprF Cys324 it is most likely that the loss
257 of gliding in this background is due to the low levels of SprF-GldK disulfide links.

258

259 **GldK Cys343 is required for Type 9 protein export**

260 Our findings demonstrate that Cys343 in GldK is essential for gliding motility,
261 functioning through the formation of a disulfide bond that attaches the SprF-SprB
262 adhesin complex to the gliding track. Remarkably, this cysteine residue is conserved
263 in the homologous PorK protein of *Porphyromonas gingivalis* even though this
264 organism is non-motile and does not utilize gliding adhesins (**Fig. 3a**). Indeed, this
265 cysteine residue is completely invariant across GldK/PorK proteins. This strongly
266 suggests that this conserved cysteine has a role(s) beyond anchoring adhesin carrier
267 proteins. More specifically, since PorK is part of the *P. gingivalis* T9SS[27], it suggests
268 that the conserved cysteine is involved in Type 9 protein export.

269 To test this hypothesis, we asked whether GldK Cys343 is required for Type 9 protein
270 secretion in *F. johnsoniae*. We found that removal of this residue completely abrogated
271 the export of a model T9SS Type A substrate protein (**Fig. 3g**). It also phenocopied
272 the effects of removing GldK or the T9SS translocon SprA on the secreted proteome,
273 which is dominated by Type A T9SS-secreted proteins[10] (**Fig. 3h**). By contrast, and as
274 noted previously above, removal of Cys343 reduces rather than completely blocks
275 export of the Type B T9SS substrate SprB (**Fig. 3d**). Thus, these experiments confirm
276 the hypothesis that GldK Cys343 is involved in Type 9 protein export in *F. johnsoniae*,
277 in addition to gliding motility, and that it is essential for the secretion of Type A
278 substrates. Control experiments using SprF variants lacking the twin-cysteine motif
279 confirm that the requirement for GldK Cys343 in Type 9 transport is independent of
280 the disulfide bond that GldK Cys343 makes with SprF (**Extended Data Fig. 3**).

281

282 **GldK Cys343 forms a disulfide bond with the T9SS component PorG**

283 The established mechanistic function of GldK Cys343 in gliding motility is to form a
284 disulfide bond with a cysteine in a partner protein (SprF). It was, therefore, highly likely
285 that its role in Type 9 protein secretion is also to form a disulfide linkage with a partner
286 protein(s), in this case presumably a T9SS component. Indeed, a possible additional
287 disulfide-bonded GldK adduct could be distinguished after NEM treatment of cells as
288 a faint band in some high exposure GldK immunoblots. This is most clearly seen in
289 the example shown in **Extended Data Fig. 4.**

290 Analysis of known T9SS components identified the protein PorG as the most likely
291 candidate to partner GldK. *F. johnsoniae* PorG (Fjoh_1692, hereafter $PorG_{Fj}$) is
292 predicted to be an 8-stranded OM protein in which the periplasmic C-tail contains the

293 same vicinal Cys-Xaa-Cys motif used by SprF to form a disulfide bond with GldK (**Fig.**
294 **4a**). The presence of cysteine residues in the PorG tail is a conserved feature across
295 the T9SS-containing Bacteroidota, although the number, spacing, and positioning of
296 the residues varies (**Fig. 4a**). For example, *P. gingivalis* PorG (PG0189 in strain W83,
297 hereafter $PorG_{Pg}$) contains a single cysteine that aligns with the second cysteine in the
298 *F. johnsoniae* $PorG_{Fj}$ motif (**Fig. 4a**). $PorG_{Pg}$ was identified as an essential T9SS
299 component in *P. gingivalis*[38,39] but its mechanistic role is unknown. Importantly, $PorG_{Pg}$
300 has been reported to co-purify with the *P. gingivalis* PorKN Hub Complex[32], an
301 observation which is consistent with the hypothesis that PorG is a disulfide-linked
302 partner of GldK/PorK.

303 We constructed a *porG* deletion mutant in *F. johnsoniae* and used this to confirm
304 that PorG is part of the T9SS in this organism. Specifically, PorG is essential for the
305 secretion of both Type A substrates and the Type B substrate SprB (**Fig. 4b-d**). The
306 $porG_{Fj}$ deletion mutant was also unable to glide, consistent with its inability to export
307 the SprB glding adhesin (**Fig. 4e**). Control experiments confirmed that the absence of
308 $PorG_{Fj}$ did not affect cellular levels of the key T9SS and gliding components SprA
309 (T9SS translocon), GldK, or SprF (**Extended Data Fig. 5b**).

310 We next tested whether the C-tail Cys_{225}-Xaa-Cys_{227} motif was important for *F.*
311 *johnsoniae* PorG function. Type A protein export and gliding motility were fully blocked
312 in the absence of the cysteine pair (**Fig. 4b,d,e**). However, partial export of the Type
313 B substrate SprB still occurred (**Fig. 4c**). This is in contrast to the phenotype of a full
314 $PorG_{Fj}$ deletion (**Fig. 4c**), but equivalent to the phenotype obtained after deleting the
315 GldK Cys343 to which we propose $PorG_{Fj}$ binds (**Fig. 3d**). Removal of Cys225 alone
316 was sufficient to almost completely block export of a model Type A substrate, whereas
317 removal of Cys227 had no substantive effect on this process (**Fig. 4b**), indicating that

318 Cys225 is the more important of the two cysteine residues. Export of the Type B
319 substrate SprB and gliding motility were either not (Cys227), or only slightly (Cys225),
320 sensitive to the loss of the individual cysteine residues (**Fig. 4d,e and Extended Data**
321 **Fig. 5a**). Overall, the phenotypic effects of Cys225 removal are more severe than
322 those of Cys227 loss.

323 Having established that the $PorG_{Fj}$ cysteine motif is required for $PorG_{Fj}$ function we
324 next investigated whether this motif was involved in forming the predicted interaction
325 with GldK Cys343. In order to detect $PorG_{Fj}$ by immunoblotting we introduced an
326 ALFA-tag into loop 3 of $PorG_{Fj}$. This epitope tag did not affect the expression, stability,
327 or functionality of $PorG_{Fj}$, and epitope-tagged cysteine motif variants showed the same
328 patterns of functional defects as the untagged proteins (**Extended Data Fig. 5c-e**).
329 Treatment of cells with NEM trapped a proportion of the $PorG_{Fj}$ molecules in a
330 disulfide-linked adduct (**Fig. 4f**) of the same size as the additional, non-SprF, adduct
331 of GldK detected in **Extended Data Fig. 4**. This adduct was absent in a *gldK* deletion
332 mutant (**Fig. 4f**) confirming that GldK is the partner protein to which $PorG_{Fj}$ is disulfide-
333 linked. Removal of GldK Cys343, but not Cys285, also blocked formation of the $PorG_{Fj}$
334 adduct confirming that GldK uses the same cysteine residue to form disulfide
335 crosslinks with both $PorG_{Fj}$ and SprF (**Fig. 4f**). Formation of the $PorG_{Fj}$-GldK adduct
336 required the presence of the twin-cysteine motif in $PorG_{Fj}$ demonstrating the
337 involvement of these residues in the disulfide linkage (**Fig. 4f**). When the $PorG_{Fj}$
338 cysteines are individually removed the adduct is still observed (**Fig. 4f**) indicating that
339 either of the cysteines can form a bond with GldK. Nevertheless, in both cases the
340 levels of the $PorG_{Fj}$-GldK adduct are lower than in the wild type, with the larger effect
341 of Cys225 removal suggesting that Cys225 is preferentially involved in forming the
342 inter-subunit disulfide bond in agreement with the greater functional importance of this

343 cysteine. Removal of either of the $PorG_{Fj}$ cysteine residues results in the $PorG_{Fj}$-GldK
344 adduct being detected even in the absence of NEM treatment (**Fig. 4f**) suggesting that
345 in these variants the disulfide bond with GldK is stabilised because it cannot be
346 attacked by the missing $PorG_{Fj}$ cysteine. Disulfide bond formation between PorG and
347 GldK does not require T9SS activity (**Extended Data Fig. 5f**).

348 Overall, the disulfide-bonding behaviours of the twin-cysteine motifs of $PorG_{Fj}$ and
349 SprF are comparable, although with $PorG_{Fj}$ there is less differentiation between the
350 roles of the two cysteines. Consequently, we interpret the behaviour of the $PorG_{Fj}$
351 cysteines in an analogous way to the SprF motif (**Fig. 3f**). Specifically, we envisage
352 that an intramolecular disulfide bond is formed between $PorG_{Fj}$ Cys225 and Cys227
353 during $PorG_{Fj}$ biogenesis, that this bond is subsequently attacked by GldK Cys343 to
354 form a disulfide linkage with $PorG_{Fj}$ (preferentially involving Cys225). In the absence
355 of either one of the $PorG_{Fj}$ cysteines formation of the disulfide bond with GldK relies
356 on adventitious oxidants and is inefficient.

357 We then examined the effects of altering the $PorG_{Fj}$ twin-cysteine motif on the
358 motions of fluorophore-tagged SprB adhesin molecules. Adhesins still moved in
359 continuous helical trajectories when $PorG_{Fj}$ lacked either one or both cysteine residues
360 (**Fig. 4g and Supplementary Video 3**) showing that adhesin movement on the tracks
361 does not require the disulfide link between $PorG_{Fj}$ and GldK. Thus, the gliding defects
362 in some of these mutants are most likely to be due to their reduced levels of adhesin
363 export (**Fig. 4c**, also evident by the larger proportion of rapidly diffusing non-exported
364 molecules in the periplasm of these strains in **Supplementary Video 3**) rather than
365 loss of adhesin function. An appreciable fraction of the adhesin trajectories in all three
366 *$porG_{Fj}$* cysteine mutants showed mid-cell reversals rather than travelling fully to the
367 next pole. Examples are shown in **Fig. 4g and Supplementary Video 4**. This

368 behaviour is very rare in wild-type cells[20] suggesting that track morphology is
369 perturbed in the cysteine mutants and that $PorG_{Fj}$ may have a role in determining the
370 architecture of the gliding tracks.

371 As noted above, the $PorG_{Fj}$ cysteine motif is not rigidly conserved. For example,
372 the PorG protein of *P. gingivalis* is missing the cysteine residue that in *F. johnsoniae*
373 PorG forms the disulfide bond with GldK (**Fig. 4a**) raising the question as to whether
374 the remaining cysteine residue (Cys232) is required to support Type 9 function. We
375 found that removing this residue abolished Type 9 export in *P. gingivalis,* as judged by
376 the loss of colony pigmentation that is characteristic of T9SS-defective strains grown
377 on blood agar[40] (**Fig. 5a,b**). Thus, the single cysteine motif of *P. gingivalis* PorG is still
378 an essential requirement for Type 9 protein secretion. Generalising this observation
379 implies that all PorG C-tail cysteine motifs are involved in PorG function but that there
380 is flexibility in the exact complement and arrangement of the cysteine residues.

381

382 **Structure of the *P. gingivalis* PorKN Hub Complex**

383 The work reported here shows that the *F. johnsoniae* protein GldK and its *P.*
384 *gingivalis* equivalent PorK are disulfide-linked to partner proteins in the OM protein.
385 Whilst PorK is known to be a component of the *P. gingivalis* Hub complex, we find that
386 the equivalent GldK protein is part of the mobile *F. johnsoniae* gliding track. This
387 implies that that the Hub complex and gliding track are related structures, and thus
388 that both are mobile tracks. From this standpoint the Hub is a miniature circular
389 analogue of the longer gliding track.

390 We sought to understand the structure of these Bacteroidota mobile tracks and to
391 characterize the structural context of the disulfide link between GldK/PorK and their

392 partner OM proteins. Since we and others[18] have been unsuccessful in isolating the
393 gliding tracks from *F. johnsoniae* we concentrated our efforts on the *P. gingivalis* PorKN
394 complex which has previously been characterized at low (>40 Å) resolution by cryo-
395 EM[32]. We were able to improve the structure of the ~3 MDa PorKN ring to near-atomic
396 resolution (2.4 Å) (**Fig. 5c**, **Extended Data Figs. 6 and 7a**, **SI Table 1**). The PorK
397 subunit is structurally defined from Gly32 to Phe476 and thus missing the 8 N-terminal
398 residues and 15 C-terminal residues of the mature protein. PorN is defined from Thr47
399 to Trp299 and so is missing the 22 N-terminal residues and 62 C-terminal residues of
400 the mature protein (**Fig. 5d**). Two glycosylation sites are present on each subunit,
401 providing glycosylation on both the outer (PorK-linked) and inner (PorN-linked) faces
402 of the ring (**Fig. 5d**).

403 The PorKN ring is composed of multiple side-by-side PorKN heterodimer units (**Fig.**
404 **5c**), consistent with earlier biochemical evidence for an equimolar PorK:PorN
405 stoichiometry[32]. The actual number of repeats is not fixed, ranging from 31 to 35 PorKN
406 heterodimers, but is most frequently 33 (**Fig. 5c**), in agreement with the earlier lower-
407 resolution study of the complex which reported 32 to 36 repeating units[32]. Such
408 variation in subunit stoichiometry is commonly observed for ring complexes made up
409 from large numbers of repeating subunits[41,42], reflecting the small differences in
410 stability of oligomers of closely similar size.

411 The overall shape of the PorKN complex is consistent with earlier lower resolution
412 cryoEM and *in situ* cryoET studies of the complex[32-34], and our high resolution structure
413 is readily fit into the published lower-resolution envelopes for the complex (**Fig. 5e**).
414 The wall of the ring is angled inwards and is almost triangular in cross-section, with
415 the outer face more sloped than the inner (**Fig. 5f**). The 33-mer ring has an outer
416 diameter of 540 Å and an inner diameter of 380 Å (**Fig. 5c**). Published cryoET images

417 (and the fit of our model to these data, **Fig. 5e**) suggest that the face of the ring formed
418 by the base of the triangle is positioned next to the OM[33,34]. Consistent with this
419 assignment, the detergent micelle in our structure lies above this face of the ring and
420 is appropriately positioned to interact with the lipidated N-termini of the PorK subunits
421 (**Fig. 5c**). This membrane-facing side of the ring is noticeably flat (**Fig. 5c**) and not
422 highly charged, as would be appropriate for a surface that moves across the face of
423 the membrane. PorK and PorN form distinct layers of the ring (**Fig. 5c**), as previously
424 speculated[32]. The positions of the PorN subunits are somewhat offset relative to PorK,
425 resulting in each PorN subunit contacting two PorK subunits and vice versa. The
426 contacts between all neighbouring subunits are tightly packed and very extensive, with
427 the interactions between the well-folded subunit cores augmented by a long N-terminal
428 arm extended by each PorK subunit across the clockwise-adjacent (as viewed from
429 the OM) PorK molecule and shorter arms at the termini of the PorN subunits which
430 contact adjacent PorK molecules (**Fig. 5g**). These extensive contacts bury more than
431 ~5,500 $Å^2$ of surface for every PorKN pair incorporated into the ring (**Fig. 5h**). This
432 large interaction interface indicates a very stable complex in which the subunit
433 interactions are rigidly fixed. Likewise, the bulk of the individual subunits are compactly
434 folded implying they are rigid structures and there are no indications of conformational
435 flexibility anywhere within the ring in the cryoEM data. These observations are difficult
436 to reconcile with earlier interpretations of cryoET data as showing a 40° variation in
437 PorKN angle driven by the PorLM motors[33].

438 The core of the PorK subunit has an extensively elaborated sulfatase-modifying
439 enzyme (SME) fold[43], as previously noted[29], and contains the canonical disulfide bond
440 and bound metal atom (that we identify as a calcium ion based on the observed co-
441 ordination, **Extended Data Fig. 7b**) [43] that likely structurally stabilize the fold. The

442 extensions to the SME core found in PorK are involved in extensive interactions with
443 neighboring subunits, adding to the stability of the ring (**Fig. 5g**).

444 The PorN subunits have a well-folded core as seen in an earlier crystal structure of
445 this part of the subunit (RMSD 0.7 Å across 169 residues)[44]. However, both the N and
446 C-termini become ordered in assembling the ring, with the N-terminus packing against
447 PorK and the C-terminus packing on the inner face of the PorN portion of the ring (**Fig.**
448 **5f,g**).

449 The PorG-reactive cysteine residue Cys356 is exposed on the OM-facing side of
450 PorK, congruent with its role in interacting with the OM-embedded PorG, and is located
451 at the inner rim of the PorKN ring (**Fig. 5g,i**). Cys356 is found in a conserved Arg-Gly-
452 Cys-Phe motif (**Fig. 3a**) with the arginine presented at the apex of a small surface loop
453 that projects away from the protein core and is stabilized by intra-loop backbone
454 hydrogen bonds. Within this loop the side chain of Arg354 sits above Cys356 partially
455 screening it from interacting partners (**Fig. 5i**) although the cysteine side chain remains
456 highly solvent exposed.

457 We used AF3 to model the interaction between PorG and PorKN. AF3 recapitulated
458 the structure of PorKN well (RMSD 2.8 Å overall for a 3:3 heterocomplex, **Extended**
459 **Data Fig. 7c**) and demonstrated that interactions between PorG and the ring are likely
460 limited to the linking disulfide bond and interactions from residues immediately
461 surrounding the disulfide in the unstructured tail of PorG (**Extended Data Fig. 7d**). In
462 particular, no consistent or high confidence interactions were predicted between the
463 base of the PorG barrel and the upper surface of the ring. We also used AF3 to predict
464 interactions between the PorM dimer arm of the PorLM motor that energizes the
465 PorKN ring (**Extended Data Fig. 7e**). The tip of the PorM dimer is predicted to lie

466 within the cleft formed between neighbouring copies of PorN at the periplasmic face
467 of the ring, with the majority of the contacts coming from one copy of the D4 domain
468 of PorM. Although the surface buried in this interaction is not substantially conserved
469 and the confidence metrics for this mode of interaction weak, this may reflect the
470 dynamic nature of the interaction between PorM and the PorKN ring. Previous
471 biochemical and genetic interaction data had suggested that PorM interacts with both
472 PorN and PorK[44-46] but only PorN contacts are supported by our modelling.

473

474 **Model for the *F. johnsoniae* gliding track structure**

475 Having established that AF3 reliably predicts the experimental structure of the
476 PorKN `mini-track' we used AF3 to predict the structure of the analogous *F. johnsoniae*
477 gliding track. These predictions included the `Hub' proteins GldK and GldN, as well as
478 the previously established gliding track component GldJ. Predictions containing equal
479 numbers of GldK, GldN, and GldJ protomers formed a high confidence and well-
480 packed filamentous structure (**Fig. 6a**). Within this filament the GldKN subunits have
481 essentially the same arrangement as the equivalent subunits in the *P. gingivalis* PorKN
482 structure (231 core residue superimpose with an RMSD of 0.7A).The GldJ subunits,
483 which are structurally related to GldK[24,35], mimic the organisation and placement of the
484 GldK protomers but are on the opposite side of the filament and run in the reverse
485 direction along the filament. The result is that GldK and GldJ pack alongside each
486 other in two antiparallel lines on the OM-proximal side of the filament with both
487 subunits in contact with GldN. The packing between all three types of subunits is
488 extensive and indicative of a single stable entity consistent with the idea that the
489 filament represents the gliding track and that GldK and GldN are components of the

track. In our model the SprF/PorG-interacting Cys343 of GldK is positioned at the centre of the OM-facing surface of the filament at the interface between the lines of GldJ and GldK subunits (**Fig. 6a**). Our model for the interactions between GldJ and GldK differs from a recent proposal based on computational docking[26].

Discussion

This work reveals a novel cellular mechanism of mechanical energy transduction in which membrane proteins are linked by disulfide bonds to a moving track structure (**Fig. 6b,c**). To the best of our knowledge such a use of disulfide bonds to attach client proteins to moving elements of a machine has no analogy in any other mechanical system in biology. Remarkably, we find that this mechanism of energy transduction is shared between two of the major phylum-specific systems of the Bacteroidota – gliding motility and Type 9 protein transport – revealing that these processes are mechanistically and evolutionarily linked (**Fig. 6b,c**).

The key observation underpinning our conclusions is the unexpected discovery that the OM-spanning protein SprF - which links the cell surface gliding adhesin SprB to the internal gliding track - is disulfide-bonded to the periplasmic lipoprotein GldK. Since almost all the SprF molecules in the cell have this disulfide linkage (**Figs. 2a,b and 3c**), and almost all are carrying adhesins along the gliding tracks (**Figs. 1e,3e, and 4g and Supplementary Video 1**), we were able to deduce that GldK must be a component of the track. This conclusion overturns the current model for the gliding apparatus in which GldK is considered to be a component of a Hub complex that links the gliding motors to the gliding tracks[16,25,26] (**Fig. 1a**). In our new model GldK, and its Hub partner GldN, are integral components of the gliding track (**Fig. 6c**), a possibility

514 that has been briefly considered by some authors[5]. Several additional lines of
515 evidence support this new model. First, AF3 modelling predicts a high-confidence
516 equimolar complex between the Hub proteins GldK and GldN and the known track
517 protein GldJ. The resulting complex is stabilised by extensive tight packing between
518 all three of the constituent protomer types, and the proteins are arranged in a repeating
519 filament-like structure as expected of the track (**Fig. 6a**). The predicted complex is
520 unlikely to represent the interfacial contact between the outside of the rotating Hub
521 and the track filament that is envisaged in the current rack-and-pinion-model of
522 gliding[25,26] because the structure prediction places the GldJ 'track' (rack) on the
523 equivalent of the inner, rather than outer, face of the PorKN ring (**Fig. 6a**). Second, the
524 previously observed stabilisation of GldK by GldJ[47] is better interpreted in terms of
525 GldK forming part of a GldJ-containing gliding track than GldK being part of a separate
526 Hub complex that does not contain GldJ. Third, a SprF variant (Cys324Ala) that we
527 infer cannot easily reverse its attachment to GldK is still able to move helically for
528 multiple circuits of the cell, implying that it must be attached to GldK throughout those
529 circuits (**Figs. 1e, 2a and Supplementary Video 1**). Finally, the fact that only SprF
530 molecules that can form a disulfide link with GldK are able to mediate continuous
531 helical movement of adhesins along the tracks (**Figs. 1e and 3e and Supplementary**
532 **Video 1**) is also consistent with GldK being part of the track.

533 Our new model for the organisation of the gliding track changes our understanding
534 of how Type 9 transport is energised in both gliding and non-gliding Bacteroidota. In
535 gliding Bacteroidota the T9SS translocon is now inferred to be energised directly by
536 the gliding track (**Fig. 6c**) rather than by a separate Hub complex (**Fig. 1a**) while the
537 Hub complex of non-gliding bacteria can now be understood to be a moving track
538 structurally analogous to the gliding track (**Fig. 6b**).

539 We envisage that the disulfide bond between SprF and the track provides a very
540 stable linkage that allows the track to exert force on those adhesin molecules that are
541 bound to the external substratum in order to propel the cell forward (high load). Even
542 under the low load conditions used in our experiments, where the cells are suspended
543 in agarose rather than pushing against a surface, the very long (~200nm) [18] SprB
544 adhesins may still require substantial force to move them through the medium
545 surrounding the cell and, thus, still show strong dependence on the presence of the
546 SprF-GldK disulfide linkage. SprF is still able to interact transiently with the gliding
547 track even in the absence of the disulfide linkage to GldK (**Figs. 1e and 3e and**
548 **Supplementary Video 1**). These weak interactions may be required for initial complex
549 formation between SprF and GldK to allow subsequent disulfide bond creation.

550 We found that PorG, an essential component of the T9SS, is also disulfide-bonded
551 to the track. Although PorG and SprF both bind to the same cysteine residue in GldK,
552 it is unlikely that their binding is competitive because GldK is in large molar excess
553 over either protein (**Fig. 2a and Extended Data Fig. 4**). The presence of a disulfide
554 linkage between PorG and GldK suggests, by analogy to SprF, that PorG moves on
555 the gliding track and that this movement results in the exertion of considerable
556 mechanical force, necessitating covalent attachment to the track. The energy-requiring
557 step in Type 9 transport is the ejection of carrier protein-substrate complexes from the
558 T9SS translocon[11] and so we speculate that the role of PorG might be to transmit force
559 from the Energy Chain to push carrier proteins out of the translocon. Intriguingly, we
560 find that cells that fail to make a disulfide connection between PorG and GldK show
561 apparent alterations in long-range track morphology (**Fig. 4g**) suggesting that PorG
562 also has a role in track placement, perhaps by displacing other OM proteins from the
563 track path. Export of the Type B T9SS substrate SprB is more strongly affected by

564 removal of PorG protein than by blocking its ability to disulfide bond with GldK (**Fig.**
565 **4c,g**). This indicates that PorG, like SprF, possesses disulfide-independent
566 interactions, potentially with the gliding track.

567 The disulfide linkages characterized here appear to be the only known instances of
568 permanent inter-molecular disulfide bonds between periplasmic proteins. This
569 probably reflects the fact that disulfide bonds are normally introduced into individual,
570 unfolded nascent polypeptides as they enter the periplasm and are thus intramolecular
571 in nature[48,49]. It may be for this reason that *F. johnsoniae* adopts a strategy of
572 introducing intramolecular disulfide linkages into SprF and PorG during their
573 biogenesis that can later be used as `donor' disulfides in the formation of the GldK-
574 SprF linkage (**Fig. 3f**). This strategy is, however, not applicable to *P. gingivalis* PorG
575 because this protein contains only a single cysteine residue. We note that the PorG-
576 reactive cysteine in the *P. gingivalis* PorKN complex is highly exposed relative to the
577 *F. johnsoniae* gliding track (**Figs. 5b,c and 6a**) which might, instead, provide sufficient
578 accessibility to allow periplasmic thiol-oxidising proteins to form the disulfide link with
579 PorG *in situ*. It is also possible that the presence of the second cysteine in the *F.*
580 *johnsoniae* PorG and SprF proteins allows the disulfide link with GldK to be reversibly
581 broken under some circumstances (**Fig. 3f**), for example to allow PorG and SprF to
582 move between tracks or temporarily detach at track crossings, but that this is not
583 required in *P. gingivalis* where PorG is attached to PorKN rings which operate in
584 isolation from one another[33,34].

585 Based on our revised understanding of the organisation of the Bacteroidota Energy
586 Chain determined here we infer that the T9SS initially evolved as part of the
587 Bacteroidota gliding machinery in order to place gliding adhesins onto the cell surface
588 (**Fig. 6c**). This ancestral function would explain why Type 9 transport uses a very

589 unusual mechanism in which exported proteins initially form a complex with an OM
590 carrier protein - an appropriate strategy for the biogenesis of cell surface adhesins -
591 rather than being directly transferred into the extracellular environment. Placing the
592 gliding track next to the translocon in order to accept the newly transported adhesin-
593 carrier protein complexes would have provided the translocon with a ready-made
594 energy source to power adhesin export. We propose that the ability to glide was
595 ancestral in the Bacteroidota but that this capability has been lost in most commensals.
596 In these non-gliding bacteria, such as *P. gingivalis*, the mobile track no longer has a
597 gliding function but is still retained in order to power the Type 9 translocon. This more
598 limited function allowed the cell to miniaturize the track in the form of the PorKN ring
599 (**Fig. 6b**). The suggested evolutionary relationship between the gliding motility
600 machinery and Type 9 protein transport has parallels with the relationship between the
601 nanomachines constituting the bacterial flagellum (a motility system that exports its
602 own components) and Type 3 Secretion Systems (which possesses only the secretion
603 function) [50].

604 Our structure of the *P. gingivalis* PorKN Hub/mini-track shows that is has no
605 substantive conformational flexibility. This suggests that force exerted on the Hub by
606 the motor complexes cause it to rotate in place as a rigid body carrying any attached
607 partner proteins with it (**Fig. 6b**). The GldJKN filaments would move linearly in a very
608 similar manner to the PorKN ring, with the GldN subunits providing closely spaced
609 contacts all along the filament for the gliding motors to push on (**Fig. 6c**). These track
610 movements would then drag the disulfide-linked partner proteins through the OM.

611 **Acknowledgments:**

612 We thank James Horne for producing the PorN and GldJ antisera and F.
613 *johnsoniae* Δ*gldK* and Δ*porG* mutants, Mark McBride for providing SprF and GldK
614 antisera, Frederick Lauber for producing the Δ*sprF* mutant, Kevin Foster for access to
615 anaerobic culture and imaging facilities, and James Garnett, Mark Roberts, Joseph
616 Aduse-Opoku, Michael Curtis, and Graham Stafford for strains, reagents, and advice
617 on working with *P. gingivalis*. We acknowledge the use of Oxford Micron Advanced
618 Imaging Facility. This work was supported by European Research Council Advanced
619 Award 833713 (BCB), Biotechnology and Biological Sciences Research Council grant
620 BB/S007474/1 (BCB and SML), and a Medical Research Council studentship to RJ.
621 This research was supported in part by the Intramural Research Program of the NIH.

622

623 **Author Contributions**

624 XL carried out all genetic and biochemical experiments, with the exception that MA
625 purified the PorKN complex. JCD, CL, and SML collected electron microscopy data
626 and determined all structures. RJ and XL carried out fluorescence microscopy
627 experiments. XL, BCB, and SML conceived the project. BCB and SML secured
628 funding. The draft manuscript was written by XL and BCB. All authors interpreted data,
629 produced figures, and revised the manuscript.

630

631 **Competing interests**

632 The authors declare no competing interests.

633

634 # Methods

635 ## Bacterial strains and growth conditions

636 All strains used in this work are listed in Supplementary Table 2.

637 *F. johnsoniae* was routinely grown aerobically in Casitone Yeast Extract (CYE)
638 medium[51] at 30 °C with shaking. For some physiological studies the cells were cultured
639 in Motility Medium (MM) [52] or PY2 medium[53].

640 *P. gingivalis* was grown anaerobically (5 % CO_2, 5 % H_2, 90 % N_2) at 37 °C in a Don
641 Whitley Scientific A45 workstation. For liquid culture *P. gingivalis* was grown in brain
642 heart infusion (BHI) medium (Oxoid) supplemented with 5 µg/ml haemin, 1 µg/ml
643 menadione, 0.5 mg/ml L-cysteine (BHIS). Culture on blood agar (BA) plates (blood
644 agar base (Oxoid), 50 µl/ml defibrinated horse blood (HB034, TCS Biosciences Ltd),
645 5 µg/ml haemin, 1 µg/ml menadione, 0.5 mg/ml L-cysteine) was used to obtain single
646 colonies. Where required, antibiotics were used at the following concentrations: 30
647 µg/ml erythromycin, 1 µg/ml tetracycline, 3 µg/ml carbenicillin (in BHIS liquid medium),
648 and 40 µg/ml carbenicillin (on BA solid medium).

649

650 ## Genetic constructs

651 Plasmids were constructed by Gibson assembly[54] or Q5 site-directed mutagenesis
652 (New England Biolabs) using the primers and target DNA in Supplementary Tables 3
653 and 4. All *F. johnsoniae* and *P. gingivalis* mutations were constructed in the native
654 chromosomal genes.

655 Chromosomal modifications were introduced into *F. johnsoniae* using the suicide
656 vector pYT313[55] harbouring the counter-selectable *sacB* gene as previously

657 described[28]. Suicide and expression plasmids were introduced into the appropriate *F.*
658 *johnsoniae* background strain by triparental mating using DH5α transformed with the
659 plasmid to be transferred and HP101 containing the helper plasmid pRK2013 as
660 previously described[51].

661 Linear DNA fragments were used for chromosomal modification in *P. gingivalis* and
662 introduced by electroporation. Electrocompetent cells were prepared from *P. gingivalis*
663 grown anaerobically to OD_{600} = 0.7. From this point manipulations were carried out
664 outside the glove box until anaerobic conditions were re-established after
665 electroporation. The cultures harvested by centrifugation at 10,000*g* for 10 min at 4°C,
666 then resuspended in ice-cold electroporation buffer (10% glycerol, 1 mM $MgCl_2$) and
667 pelleted again under the same conditions. This washing step was repeated once more
668 before resuspending the final electrocompetent cells in 200 µl of electroporation buffer.
669 Electroporation was performed by mixing the electrocompetent cells with 0.5–2 µg of
670 transforming DNA in an 2 mm electroporation cuvette (165-2086, Bio-Rad) and pulsing
671 at 2500 V for 5 ms in a BTX ECM 399 Electroporation System (SLS). Following
672 electroporation, the cuvette was returned to the glove box, supplemented with 1 ml
673 deoxygenated BHIS medium, and incubated for 24 h to allow the cells to recover. If
674 *cepA* was used as the selective marker the cultures were then diluted 1:100 in BHIS
675 supplemented with 3 µg/mL carbenicillin and incubated until turbid (5–7 days). A
676 dilution series was then plated on blood agar plates supplemented with 40 µg/mL
677 carbenicillin. For other selection markers the transformed culture was plated directly
678 onto BA supplemented with the appropriate antibiotic.

679 To facilitate genetic modification of *P. gingivalis* in a triple gingipain deleted
680 background the *rgpB*::*ermAM-F* locus in strain EK18[56] was replaced with *cepA* using
681 a SmaI-digested fragment of pCL54 to produced strain P54.

682 All plasmid constructs and chromosomal modifications were confirmed by
683 sequencing.
684

685 **Immunoblotting and antisera used.**

686 Immunoblotting was carried out as previously described[11]. Polyclonal antibodies
687 against GldJ and PorN were raised in rabbits against synthetic peptides. Polyclonal
688 antibodies against SprF[14], GldK[29], and SprA[57] were provided by Mark McBride
689 (University of Wisconsin-Milwaukee). The following commercial antisera were used:
690 anti-HaloTag (G921A, Promega), anti-GroEL (G6532 Merck), anti-mCherry
691 (ab167453, Abcam), anti-ALFA-Tag (N1582, Synaptic Systems GmbH), anti-mouse
692 IgG peroxidase conjugate (A4416 Merck), and anti-rabbit IgG peroxidase conjugate
693 (31462 Pierce).
694

695 **Analytical methods**

696 The protease protection assay for SprB export and the analysis of mCherry-CTD
697 secretion were carried out as previously described[11].

698 Measurements of gliding motility on agar and analysis of the secreted proteome
699 were performed as previously described[10].

700

701 **Whole cell analysis of disulfide-bonded protein complexes**

702 The *F. johnsoniae* strain to be analyzed was grown overnight in 5 ml CYE medium,
703 diluted 1:100 into 15 ml fresh CYE medium, and cultured until OD_{600}=0.6. Cells were
704 collected by centrifugation at 8,000*g* for 5 min, washed in PBS buffer, and

705 resuspended in PBS buffer to OD_{600}=1. The sample was aliquoted equally into two
706 0.5ml fractions which were then either supplemented or not with 5 mM *N*-
707 ethylmaleimide (E3876-5G, Merck) and incubated for 5 min in the dark on a roller at
708 room temperature. Each sample was aliquoted equally into two 0.25 ml fractions that
709 were then pelleted, washed in PBS, resuspended in PBS, and boiled for 5 min with 1x
710 SDS-PAGE sample buffer either with or without 100 mM DTT, then analyzed by
711 immunoblotting. For the protonophore treatment experiments the growing culture was
712 supplemented with 10 μM CCCP (C2759-1G, Merck) for 20 min before harvesting the
713 cells, and 10 μM CCCP was then maintained throughout the sample preparation
714 procedure.

715

716 **Live cell fluorescence microscopy**

717 *F. johnsoniae* strains were cultured in MM to OD_{600} = 0.4 and 900 μl added to an
718 Eppendorf tube containing 100 μl of MM pre-mixed with 1 μl of a 10 nM solution of
719 Janelia Fluor JFX650 HaloTag Ligand (Promega) in dimethyl sulfoxide. The tubes
720 were shaken at 30 °C for 20 min and the cells then pelleted by centrifugation at
721 7,000*g* for 3 min. The cells were washed four times by resuspension in 1 ml of PY2
722 medium and repelleting, and finally resuspended in 200 μl PY2 medium. 1 μl of this
723 cell suspension was spotted onto agarose pads formed from 1% agarose in PY2
724 medium and then imaged.

725 All imaging data were acquired on a Nanoimager (Oxford Nanoimaging) equipped
726 with a 640 nm 1W DPSS laser. Optical magnification was provided by a 100× oil-
727 immersion objective (Olympus, numerical aperture (NA) 1.4) and images were
728 acquired using an ORCA-Flash4.0 V3 CMOS camera (Hamamatsu). All fluorescence

729 images were collected at 15% laser power using 30 ms continuous exposure. Where
730 applicable, data were acquired in 3D by engaging the astigmatic lens of the
731 Nanoimager. The z-co-ordinate was calibrated by taking a z-stack in 2 nm increments
732 in the range -1 µm to +1 µm from focus, of 0.1 µm tetraspec beads (T7279, Invitrogen)
733 immobilised on a glass slide with poly-L-lysine.

734 Raw data were analysed using the Fiji plugin ThunderSTORM[58] to determine single
735 molecule localisations. Single molecule trajectories within cells were computed using
736 a custom Python script that incorporated the Trackpy package
737 (https://doi.org/10.5281/zenodo.1213240), with a memory allowance of 2 frames and
738 a search range of 3 pixels per frame. Tracks were filtered using a minimum length of
739 30 frames.

740

741 **Purification of PorKN complexes**

742 PorKN complexes were purified by modifying a previously described method[32,59].
743 The complexes were purified from a triple gingipain-deleted mutant of *P. gingivalis*
744 W50 (EK18). In this *P. gingivalis* strain PorK is PG_0288 and PorN is PG_0291. The
745 strain was grown under anaerobic conditions in 10 l of BHIS broth to an OD_{650} of 1.
746 Cells were harvested by centrifugation at 15,000*g* for 1 h. The pellet was resuspended
747 in lysis buffer (50 mM TrisHCl pH 7.5, 150 mM NaCl, 0.5 M sucrose, 5 mM $MgCl_2$, 1%
748 (w/v) n-Dodecyl β-D-maltoside (DDM)(Anatrace), benzonase (Sigma-Aldrich) and
749 cOmplete™ Protease Inhibitor Cocktail (Sigma-Aldrich)) and gently mixed using a
750 magnetic stirrer at 4 °C for 3 h. The resulting lysate was clarified by centrifugation at
751 10,000*g* at 4 °C for 1 h. Na_2EDTA was added to the clarified supernatant to a final
752 concentration of 10 mM, and then lysozyme powder (Sigma-Aldrich) was added to a

753 final concentration of 0.5 mg/ml. The mixture was then incubated at 37 °C for 45 min
754 followed by centrifugation at 210,000*g* at 4 °C for 90 min. The resulting pellet was
755 resuspended in resuspension buffer (10 mM Tris HCl pH 7.5, 500 mM NaCl, 5 mM
756 Na_2EDTA, 1% (w/v) DDM) and centrifuged at 10,000*g* at 4 °C for 15 min to remove
757 unsolubilised material. The recovered supernatant was mixed at a ratio of 1:3 with a
758 30% CsCl solution (30% (w/v) CsCl, 10 mM Tris HCl pH 7.5, 0.5% (w/v) DDM] and
759 then centrifuged at 215,000*g* at 20 °C for 19 h in a SW55 Ti rotor (Beckman-Coulter).
760 Fractions were sampled from the top downwards with a wide-bore pipette tip. 10
761 soluble fractions were isolated, followed by a loose pellet (LP) fraction containing the
762 soluble PorKN complexes, and an insoluble pellet (P) fraction. Fractions were diluted
763 at a ratio of 1:2 with dilution buffer (10 mM Tris HCl pH 7.5, 500 mM NaCl, 0.5% (w/v)
764 DDM, 5 mM Na_2EDTA) and the PorKN complexes pelleted by centrifugation at
765 210,000*g* for 2 h. The pellets were resuspended in sample buffer (10 mM Tris HCl pH
766 7.5, 500 mM NaCl, 0.5% (w/v) DDM) and successful fractionation confirmed by
767 immunoblotting using a PorN antibody. The LP fraction (400 µL) was loaded onto a
768 discontinuous sucrose gradient formed by layering equal volumes (400 µL) of,
769 successively, 2 M, 1.9 M, 1.8 M, 1.7 M, 1.6 M, 1.5 M, and 1 M sucrose in dilution buffer.
770 The gradients were centrifuged at 215,000*g* at 12 °C for 17 h in a SW55 Ti rotor
771 (Beckman-Coulter). Fractions were sampled from the top downwards with a wide-bore
772 pipette tip, 11 fractions were isolated (F1 to F11, with F1 being the upper-most
773 fraction). Fractions were diluted at a ratio of 1:2 with dilution buffer and the PorKN
774 complexes pelleted by centrifugation at 250,000*g* for 1 h 45 min. The pellets were
775 resuspended in sample buffer and then analysed by SDS-PAGE and by
776 immunoblotting using a PorN antibody to identify the fractions (typically F6 and F7)
777 containing the highest concentration of PorKN rings. These fractions were pooled and

778 pelleted at 186,000*g* for 2 h at 12 °C. The pellet was resuspended in 30 µl sample
779 buffer and used to prepare cryoEM grids.

780

781 **Cryo-EM sample preparation and imaging**

782 3 µl of the PorKN sample (A_{280nm} = 7.2) was applied to ultra-thin carbon coated
783 grids (Quantifoil 300 mesh, Au R2/1) at 4°C in 100% humidity. The sample was
784 adsorbed for 60 s, blotted 3 s, and plunge frozen in liquid ethane using a Vitrobot mark
785 IV (FEI).

786 Movies were collected in counted mode, in Electron Event Representation (EER)
787 format, on a CFEG-equipped Titan Krios G4 (Thermo Fisher Scientific) operating at
788 300 kV with a Selectris X imaging filter (Thermo Fisher Scientific) and slit width of 10
789 eV, at 165,000x magnification on a Falcon 4i direct detection camera (Thermo Fisher
790 Scientific), corresponding to a calibrated pixel size of 0.732 Å. Movies were collected
791 at a total dose of 55.0 (Table 1), fractionated to ~ 1.0 $e^{-}/Å^2$ per fraction for motion
792 correction.

793

794 **Cryo-EM data processing**

795 Patched motion correction, CTF parameter estimation, particle picking, extraction,
796 and initial 2D classification was performed in SIMPLE 3.0[60]. All downstream
797 processing was carried out in cryoSPARC[61]. Global resolution was estimated from
798 gold-standard Fourier shell correlations (FSCs) using the 0.143 criterion and local
799 resolution estimation was calculated using the 0.5 criterion.

800 The cryo-EM processing workflow for PorKN is outlined in **Extended Data Fig. 7**.
801 Briefly, particles were downsampled from 0.732 Å/pixel to 1.464 Å/pixel and subjected
802 to one round of reference-free 2D classification (k=100) using a 600 Å soft circular
803 mask. Selected particles (162,414) were further downsampled to a pixel size of 2.928
804 Å and subjected to another round of 2D classification (50 classes, no mask), yielding
805 124,099 cleaner particles. A low resolution volume was generated from these particles
806 after *ab initio* reconstruction with D33 symmetry applied. Corresponding particles were
807 then non-uniform refined (applying D33 symmetry, 10 Å lowpass filter) against this
808 volume, resulting in a Nyquist-limited 5.9 Å volume. Unmasked 3D classification of the
809 particles was then performed against 10 classes using a resolution filter of 8 Å while
810 applying D33 symmetry. Particles belonging to the most symmetric and structured
811 volume were re-extracted to a pixel size of 1.7568 Å/pixel after re-centring using prior
812 aligned shifts. This was followed by non-uniform refinement (D33 symmetry) against
813 a corresponding 10 Å lowpass-filtered volume that generated an improved 4.0 Å
814 volume. Local refinement using a rotational search extent of 5 degrees and shift extent
815 of 3 Å was performed on D33 symmetry-expanded particles (1,097,778) in C1 against
816 the corresponding map lowpass-filtered to 8 Å, using a soft mask covering multiple
817 subunit copies on the ring, resulting in a 3.5 Å Nyquist-limited reconstruction. Particles
818 and corresponding volume were then re-centred to the mask centre of mass and re-
819 extracted using these aligned shifts to a pixel size of 1.1764 Å/pixel. These particles
820 were subjected to local refinement using limited searches (5° angular, 3 Å shifts),
821 resulting in a 3.1 Å volume. Local CTF refinement followed by an identical local
822 refinement scheme further improved map quality to 2.5 Å. Particles were then re-
823 extracted using their aligned shifts to a pixel size of 1.097 Å, followed by an additional
824 round of C1 local refinement that generated a slightly improved 2.5 Å volume. Focused

825 3D classification using a mask covering three subunits on the ring was performed
826 against 4 classes in C1 and using a resolution filter of 3 Å. Particles belonging to the
827 most populated class were selected and underwent local refinement (C1), generating
828 a 2.4 Å volume from 676,608 particles.

829

830 **Model building, structure refinement, and figure preparation**

831 Iterative model building and real-space refinement using rotamer, and
832 Ramachandran restraints was performed in Coot v0.9[62] and Phenix[63], respectively.
833 Validation was performed in Molprobity[64] within Phenix. Cryo-EM data collection,
834 image processing and structure refinement statistics are listed in Supplementary Table
835 1. Figures were prepared using UCSF ChimeraX v.1.9[65].

836

837 **Statistics and reproducibility**

838 All experiments shown in the paper are representative with similar data obtained for
839 at least three biological repeats.

840

841 **Data availability**

842 Cryo-EM density maps and atomic coordinates are deposited in the Electron
843 Microscopy DataBank (EMDB) with the following accession number: EMD-48769.
844 Atomic coordinates are deposited in the Protein Data Bank (PDB) with the following
845 accession number: PDB 9MZU.

846 Gel and immunoblot source data are published alongside this paper.

https://github.com/notdrjones/Single-Particle-Tracking-for-Disulfide-Bond-Paper

Requests for materials should be addressed to BCB.

Code availability

Original code used in this study is available at https://github.com/notdrjones/Single-Particle-Tracking-for-Disulfide-Bond-Paper.

853 **Supplementary Video 1. Mobility of fluorophore-tagged SprB adhesin molecules**
854 **in *F. johnsoniae* cells with mutations in *sprF*.** Raw images were recorded with
855 continuous exposure at 33 fps using epifluorescence microscopy. Playback is in real
856 time. The area of the field of view is 32.7 x 32.7 µm.

857 **Supplementary Video 2. Mobility of fluorophore-tagged SprB adhesin molecules**
858 **in *F. johnsoniae* cells with mutations in *gldK*.** Raw images were recorded with
859 continuous exposure at 33 fps using epifluorescence microscopy. Playback is in real
860 time. The area of the field of view is 32.7 x 32.7 µm.

861 **Supplementary Video 3**. **Mobility of fluorophore-tagged SprB adhesin molecules**
862 **in *F. johnsoniae* cells with mutations in *porG*.** Raw images were recorded with
863 continuous exposure at 33 fps using epifluorescence microscopy. Playback is in real
864 time. The area of the field of view is 32.7 x 32.7 µm.

865 **Supplementary Video 4. Single particle tracking of a fluorophore-tagged SprB**
866 **adhesin molecule in a *F. johnsoniae porG*^{C225S,C227S} mutant cell showing mid-cell**
867 **reversals.** Raw images were recorded with continuous exposure at 33 fps using
868 epifluorescence microscopy. Overlaid on the image is the real time progression of the
869 super-resolution fit of the adhesin trajectory, coloured by time. The scale bar
870 represents 1 µm.

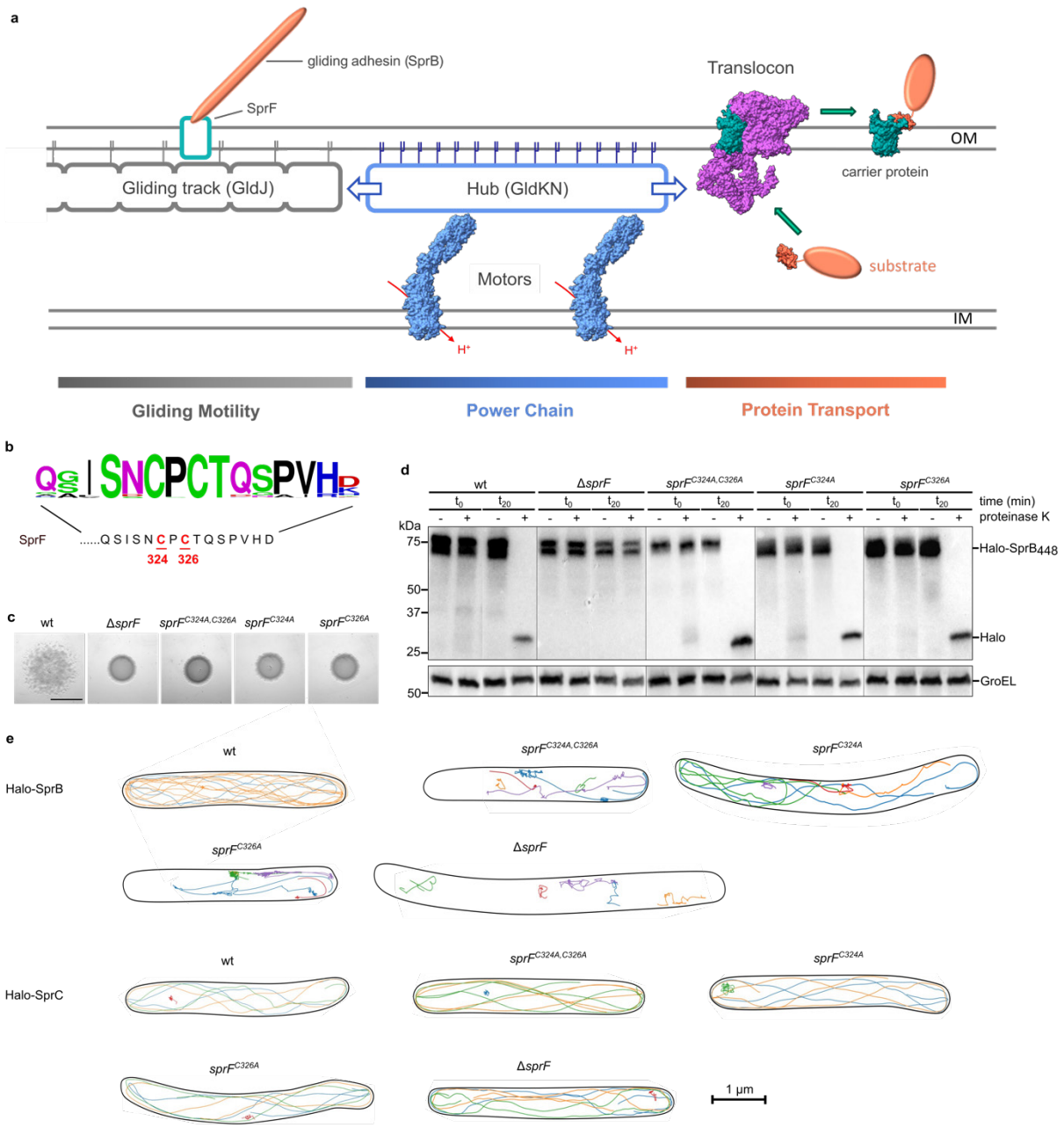

Fig. 1 | The cysteine residues in the periplasmic C-tail of SprF are essential for SprB movement and gliding motility.

a, Current model for the organization of the gliding motility apparatus and T9SS in *F. johnsoniae* involving a shared Power Train. OM, outer membrane. IM, inner membrane.

b, Sequence of the periplasmic C-tail of *F. johnsoniae* SprF with the twin-cysteine motif highlighted and a Weblogo display of the sequence conservation (500 closest whole protein homologues) above.

c-e, Characterization of *sprF* mutants with substitutions in the conserved cysteine pair. wt, wild type. Similar results were obtained for 3 biological repeats.

c, Spreading (gliding) morphology on agar. Scale bar, 5mm.

882 **d,** Cell surface exposure of the adhesin SprB assessed by protease protection. The indicated
883 strains expressing a fusion between HaloTag and the final 448 amino acids of SprB (Halo-
884 $SprB_{448}$) were incubated with Proteinase K (+ lanes). Reactions were stopped immediately (t_0)
885 or after 20 min (t_{20}) and analysed by immunoblotting with Halotag antibodies. The cytoplasmic
886 protein GroEL serves as a both a loading and cell integrity control. In each panel (which
887 correspond to separate immunoblots) a lane has been removed between the t_0 and t_{20}
888 samples.
889 **e**, Exemplar trajectories of single fluorophore-labelled HaloTag-SprB adhesin molecules or
890 HaloTag-SprC molecules in the indicated backgrounds. The trajectories link the single
891 molecule localizations in successive frames recorded for agarose-immobilised cells and are
892 2D projections of what is a 3D process. Each trajectory within a cell is shown in a different
893 colour and the segmented outline of the cell is shown in black. For the SprF cysteine variants
894 cells were chosen to illustrate the observed range of SprB mobility behaviours. See also
895 Supplementary Video 1.

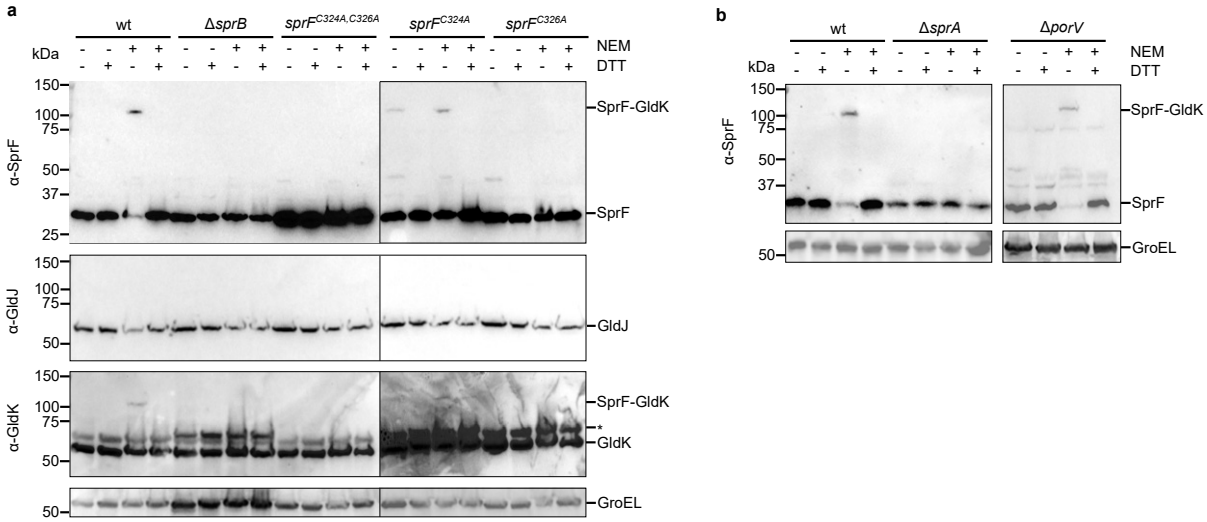

Fig. 2 | SprF forms a disulfide bond with the Hub protein GldK.

Strains with the indicated mutations were subject to whole cell immunoblotting with the specified antisera. Where indicated the cells were pre-treated with NEM. At the SDS-PAGE step samples were run under either non-reducing (- DTT) or reducing (+ DTT) conditions. GroEL serves as a loading control. *, non-specific background band. wt, wild type; a strain missing the T9SS translocon (Δ*sprA*); a strain missing the Type A carrier protein PorV (Δ*porV*). Similar results were obtained for three biological repeats.

a, SprF forms disulfide bonds with GldK but not GldJ.

b, Formation of a disulfide bond between SprF and GldK depends on Type 9 transport activity but is independent of Type A T9SS export.

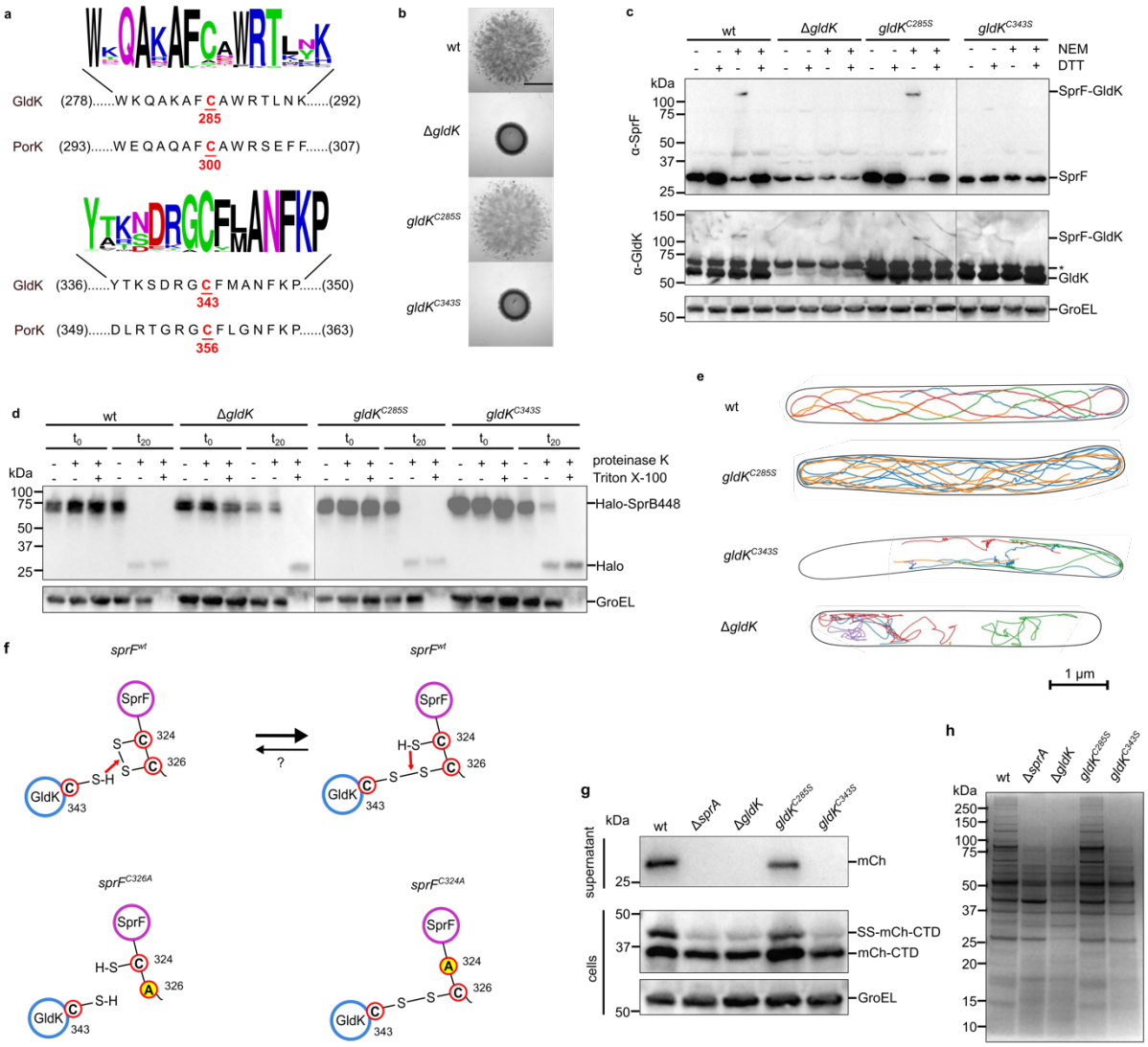

Fig. 3 | Identification and functional characterization of the SprF-crosslinking residue in GldK.

a, The sequences of the two cysteine-containing polypeptide regions of *F. johnsoniae* GldK and the corresponding regions of *P. gingivalis* PorK. Above is a Weblogo display of the sequence conservation for sequences with >40% whole protein identity to GldK.

b,c, Identification of the GldK cysteine that forms the disulfide linkage with SprF.

b, Spreading (gliding) morphology on agar. Scale bar, 5mm.

c, Strains with the indicated mutations were subject to whole cell immunoblotting with the specified antisera. Where indicated the cells were pre-treated with NEM. At the SDS-PAGE step samples were run under either non-reducing (- DTT) or reducing (+ DTT) conditions. GroEL serves as a loading control. *, non-specific background band.

d, Cell surface exposure of the Type B T9SS substrate SprB assessed by protease protection. Strains expressing a HaloTag fusion between the signal sequence and the final 448 amino acids of SprB (Halo-SprB448) in the indicated genetic backgrounds, were incubated with

925 Proteinase K and the detergent Triton X-100 as indicated. Reactions were stopped
926 immediately (t_0) or after 20 min (t_{20}) and analysed by immunoblotting with HaloTag antibodies.
927 The cytoplasmic protein GroEL serves as both a loading and cell integrity control.
928 **e**, Exemplar trajectories of single fluorophore-labelled HaloTag-SprB adhesin molecules in the
929 indicated backgrounds. The trajectories link the single molecule localizations in successive
930 frames recorded for agarose-immobilised cells and are 2D projections of what is a 3D process.
931 Each trajectory within a cell is shown in a different colour and the segmented outline of the
932 cell is shown in black. For the *gldK*^{C343S} background a cell was chosen to illustrate the observed
933 range of SprB mobility behaviours. See also Supplementary Video 2.
934 **f**, Schematic showing the proposed reactions between the cysteine residues of SprF and GldK
935 (top) and how this is altered in single cysteine SprF variants (bottom). The pink arrows
936 represent attacks by a free cysteine residue on an adjacent disulfide bond. Whether disulfide
937 bond formation between SprF and GldK is reversible under physiological conditions is
938 unknown (indicated by `?').
939 **g,h,** GldK Cys343 is required for Type 9 protein secretion.
940 **g**, Analysis of the secretion of a model Type A substrate protein comprising a fusion between
941 a signal sequence (SS), mCherry (mCh), and a T9SS-targeting C-terminal domain (CTD).
942 Cells were separated into cell and supernatant fractions and analyzed by anti-mCherry
943 immunoblotting. The successively processed forms of the fusion proteins are indicated to the
944 right of the blots. GroEL serves as a loading control.
945 **h**, Secretome analysis. Culture supernatants were separated by SDS-PAGE and stained with
946 Coomassie Blue.
947 **b-e,g,h,** Similar results were obtained for three biological repeats. wt, wild type. Δ*sprA*, a strain
948 missing the T9SS translocon.

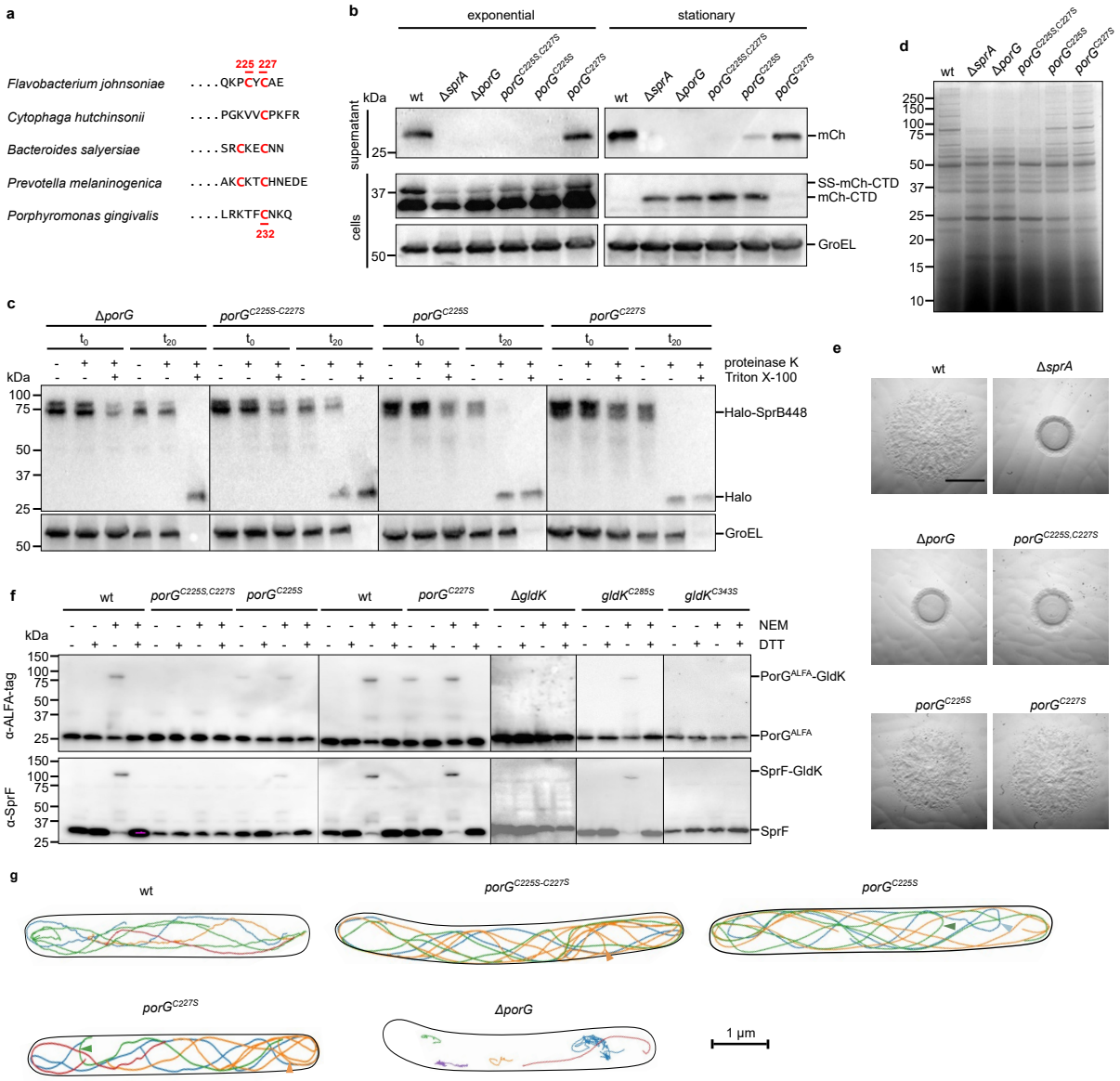

Fig. 4 | *F. johnsoniae* PorG forms a disulfide bond with GldK C343 that is essential for Type 9 protein transport and gliding motility.

a, The periplasmic C-tails of PorG proteins contain cysteine residues. Sequence alignment of representative PorG C-tails from the indicated Bacteroidota species with cysteine residues highlighted. *F. johnsoniae* and *C. hutchinsonii* are gliding bacteria, others are non-gliding species.

b-d, The Cys residues of *F. johnsoniae* PorG are required for gliding motility and Type 9 protein transport. wt, wild type. Δ*sprA*, strain missing the T9SS translocon. Similar results were obtained for 3 biological repeats.

b, Analysis of the secretion of a model Type A substrate protein comprising a fusion between a signal sequence (SS), mCherry (mCh), and a T9SS-targeting C-terminal domain (CTD). Cells were grown to exponential or stationary phase as indicated, separated into cell and

963 supernatant fractions, and analyzed by anti-mCherry immunoblotting. The successively
964 processed forms of the fusion proteins are indicated to the right of the blots. GroEL serves as
965 a loading control.
966 **c**, Cell surface exposure of the Type B substrate SprB assessed by protease protection. The
967 specified strains expressing a fusion between HaloTag and the final 448 amino acids of SprB
968 (Halo-SprB$_{448}$) were incubated with Proteinase K and the detergent Triton X-100 as indicated.
969 Reactions were stopped immediately (t_0) or after 20 min (t_{20}) and analysed by immunoblotting
970 with Halotag antibodies. The cytoplasmic protein GroEL serves as a both a loading and cell
971 integrity control.
972 **d,** Secretome analysis. The supernatants of cultures grown to stationary phase were
973 separated by SDS-PAGE and stained with Coomassie Blue.
974 **e,** Spreading (gliding) morphology on agar after 24 h growth. Scale bar, 5mm. See Extended
975 Data Fig. 5a for data at 6 h growth.
976 **f,** PorG is disulfide-bonded to GldK C343. All strains express PorG epitope-tagged by insertion
977 of ALFA-tag in loop 3. Strains were subject to whole cell immunoblotting with the indicated
978 antibodies. Where indicated the cells were pre-treated with NEM. At the SDS-PAGE step
979 samples were run under either non-reducing (- DTT) or reducing (+ DTT) conditions. *, non-
980 specific background band.
981 **g,** Exemplar trajectories of single fluorophore-labelled HaloTag-SprB adhesin molecules in the
982 indicated backgrounds. The trajectories link the single molecule localizations in successive
983 frames recorded for agarose-immobilised cells and are 2D projections of what is a 3D process.
984 Each trajectory within a cell is shown in a different colour and the segmented outline of the
985 cell is shown in black. Un-transported periplasmic SprB molecules have been edited out for
986 clarity. Arrows indicate examples of mid-cell reversals of the SprB trajectories. See also
987 Supplementary Videos 3 and 4.
988 **b-g,** Similar results were obtained from 3 biological repeats. wt, wild type.
989
990

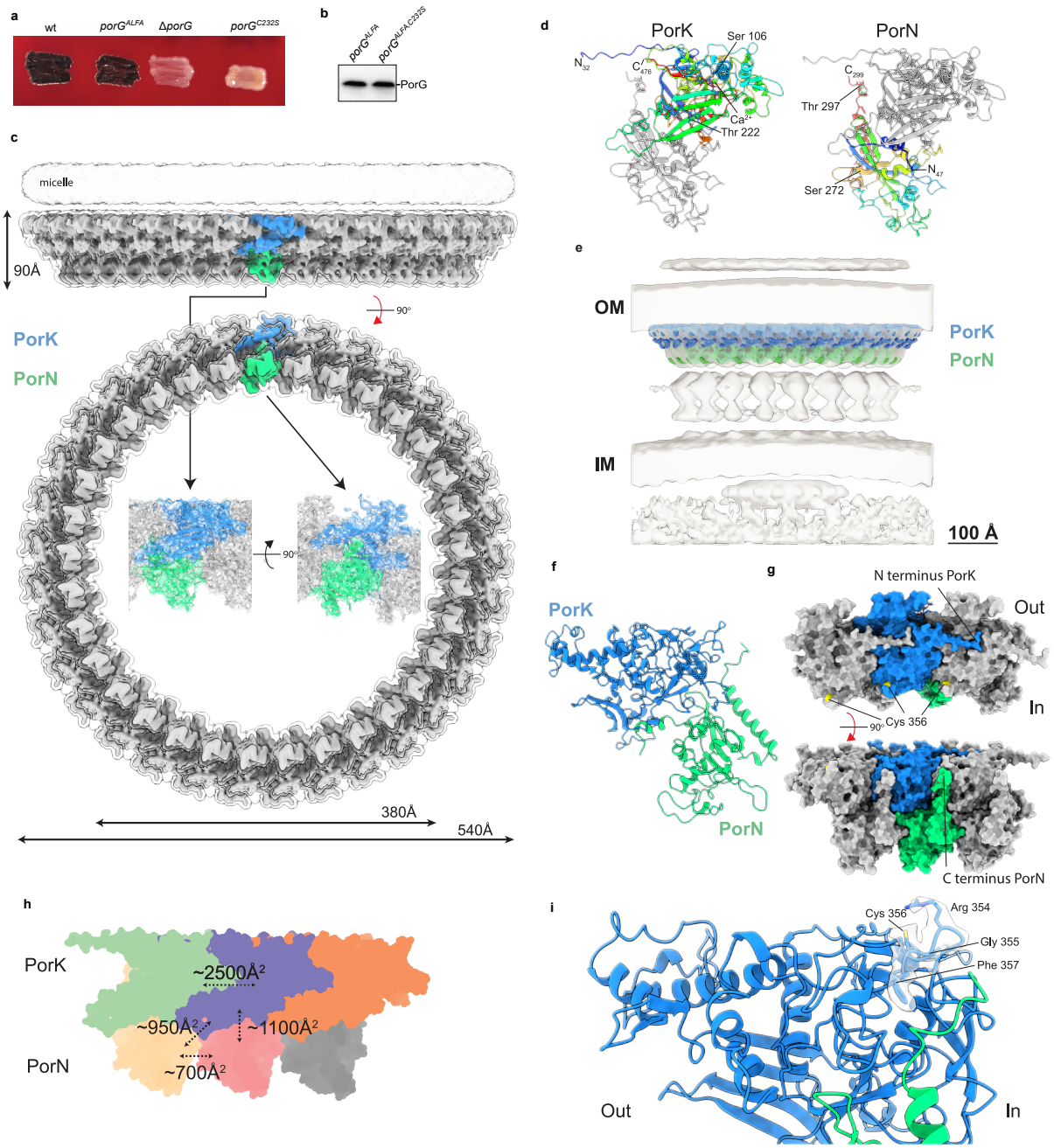

Fig. 5 | Importance of the cysteine residue of *P. gingivalis* PorG and structure of the PorKN Hub complex.

a,b, *P. gingivalis* PorG Cys232 is required for T9SS activity. Similar results were obtained from 3 biological repeats. wt, wild type. *porG*^{ALFA}, codes for PorG with an ALFA-tag epitope.

a, Strains containing the indicated *porG* alleles were grown on blood agar.

b, Equivalent strains constructed in a gingipain-deficient background were analysed by whole cell immunoblotting.

c, CryoEM volume for a 33-mer *P. gingivalis* PorKN complex at 4.0 Å resolution viewed from the side and from the periplasm. The inset shows the structure of the repeating PorKN unit

1002 obtained at higher (2.4 Å) resolution. The structure is depicted at high contour level (solid
1003 representation with a single PorKN unit shown in colour) and at a low contour level
1004 (transparent envelope) to visualize the detergent micelle which approximates the position of
1005 the OM.
1006 **d,** Structures of PorK and PorN in cartoon representation and rainbows coloured from N- (blue)
1007 to C-terminus (red), viewed from the inner rim of the PorKN ring and with the OM at Top. The
1008 bound Ca^{2+} ion is shown in atomic sphere representation. Glycosylated serine and threonine
1009 residues are labelled.
1010 **e,** The PorKN structure from **c** (coloured density) placed into the cryoET volume of the complex
1011 resolved previously in intact cells[33] (EMD-24227).
1012 **f,** View of the PorKN heterodimer unit in cartoons representation viewed from within the ring
1013 and with OM at top illustrating the triangular cross-section of the PorKN ring.
1014 **g,** Space-filling model of a PorKN pair and their immediate neighbours viewed from the OM
1015 (Top) and from the outer rim of the PorKN ring with the OM above (Bottom). The position of
1016 the PorG-reactive Cys 356 on PorK is shown (yellow).
1017 **h,** Schematic summarizing the areas buried by the different inter-subunit interfaces of the
1018 PorKN complex. Protomers are oriented as in **d**.
1019 **i,** Structure of the external loop bearing the PorG-reactive cysteine 356 of PorK with density
1020 for the motif overlaid.

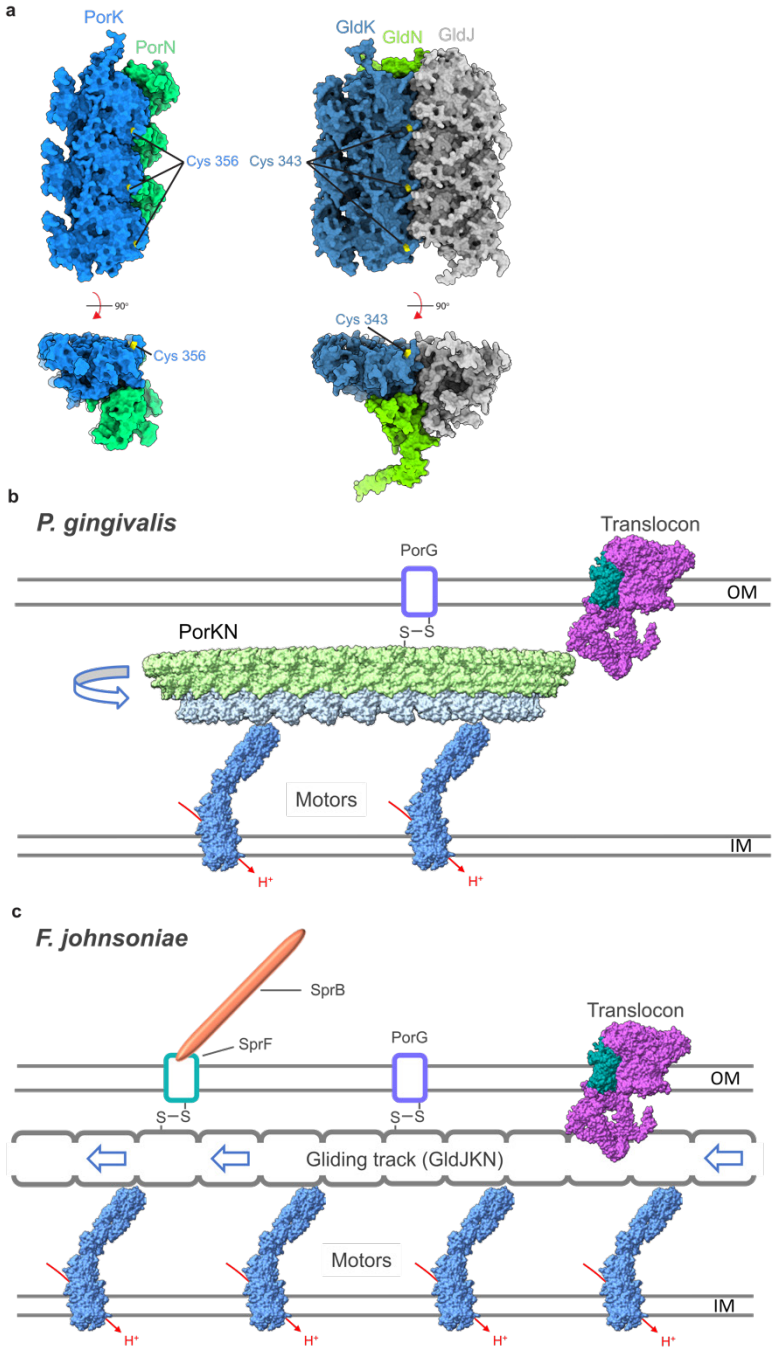

1021

1022

1023 **Fig. 6 | A new model for the connection between gliding motility and T9SS protein**
1024 **transport.**

1025 **a,** Comparison of the structure of the *P. gingivalis* PorKN ring oligomer (Left) with an AF3
1026 model for the *F. johnsoniae* GldJKN track oligomer (Right). In each case three adjacent copies
1027 of the repeating unit (PorKN or GldJKN) are shown in spacefilling representation viewed from
1028 the OM (Top) or in cross-section through the oligomer with the OM at the top (Bottom). The
1029 position of the PorG/SprF-interacting cysteines are indicated (yellow).

1030 **b,** Updated model for the organization of the T9SS in the paradigm non-gliding Bacteroidota
1031 *P. gingivalis* based on the findings in this work. The T9SS component PorG is disulfide-linked
1032 to the rotating PorKN Hub complex which energizes the translocon.
1033 **c,** Revised model for the relationship between the gliding motility apparatus and the T9SS in
1034 the paradigm gliding Bacteroidota *F. johnsoniae* based on discoveries in this work. The
1035 adhesin carrier protein SprF and the T9SS component PorG are disulfide-linked to a moving
1036 gliding track composed of GldJ, GldK, and GldN. The translocon receives energetic input from
1037 the gliding track.

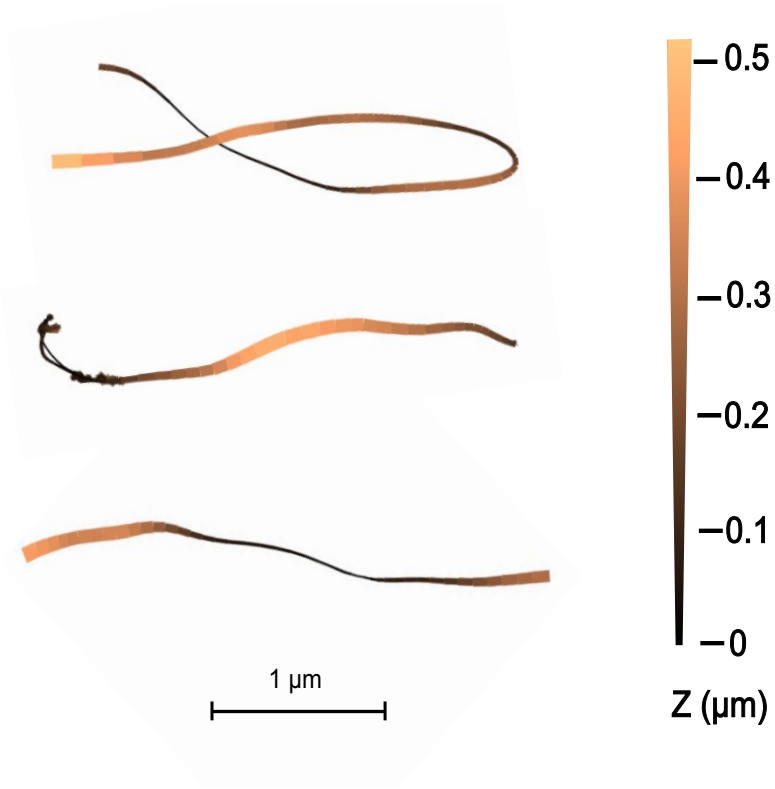

1038

1039 **Extended Data Fig. 1 | 3D single particle tracking of fluorescently-tagged SprB adhesin**
1040 **molecules in 3D in SprF cysteine-substituted variants.**
1041 The motions of single fluorophore-labelled HaloTag-SprB adhesin molecules were imaged in
1042 3D in agarose-immobilised cells of strains with single and double cysteine substitutions in
1043 SprF. The short, apparently directional trajectories present in these cells were extracted and
1044 the single molecule localizations in successive frames plotted in xy projection with the relative
1045 z position represented by variations in colour and line width as specified in the colour bar.
1046 Three representative trajectories are shown. 100 out of 100 such trajectories (from three
1047 biological repeats of the three cysteine mutants) where the handedness could be determined
1048 showed left-handed helicity consistent with the movement being on the gliding tracks.

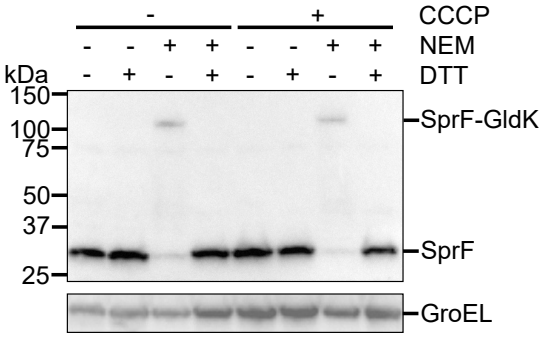

Extended Data Fig. 2 | The disulfide adduct involving SprF is stable to removal of the protonmotive force.

Immunoblots of whole wild type cells. Where indicated the cells were treated with 10 μM of the protonophore carbonyl cyanide *m*-chlorophenyl hydrazone (CCCP) for 20 min before analysis. Where indicated cells were treated with NEM. At the SDS-PAGE step samples were run under either non-reducing (- DTT) or reducing (+ DTT) conditions. GroEL serves as a loading control. Similar results were obtained from three biological repeats.

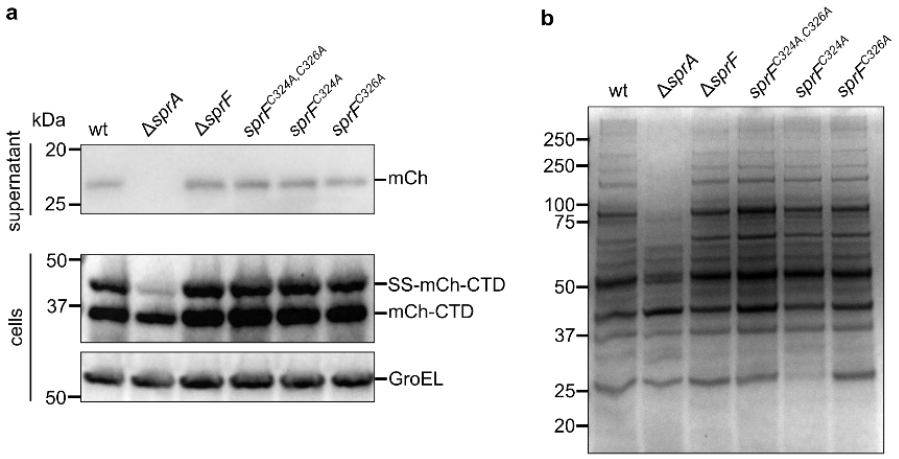

1059

1060

1061 **Extended Data Fig. 3 | The GldK-SprF disulfide linkage is not required for the secretion**
1062 **of T9SS Type A substrates.** Similar results were obtained from three biological repeats.
1063 **a,** Analysis of the secretion of a model Type A substrate protein comprising a fusion between
1064 a signal sequence (SS), mCherry (mCh), and a T9SS-targeting C-terminal domain (CTD).
1065 whole cell and supernatant samples analyzed by anti-mCherry immunoblotting. The
1066 successively processed forms of the fusion proteins are indicated to the right of the blots. The
1067 Δ*sprA* strain is missing the T9SS translocon. GroEL serves as a loading control.
1068 **b,** Secretome analysis of SprF C-tail cysteine variants. The Δ*sprA* strain is missing the T9SS
1069 translocon.

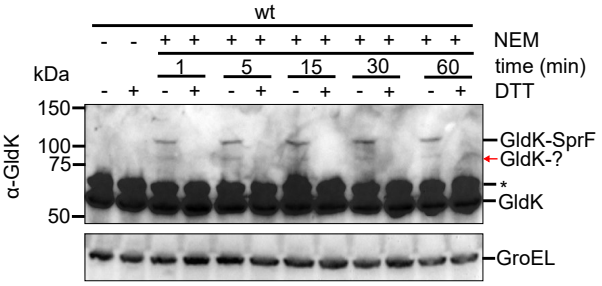

1070

1071

1072 **Extended Data Figure 4 | GldK forms disulfide linkages with SprF and another protein.**

1073 Wild type cells were subject to whole cell immunoblotting with the specified antisera. Where
1074 indicated the cells were pre-treated with NEM for the specified time. At the SDS-PAGE step
1075 samples were run under either non-reducing (- DTT) or reducing (+ DTT) conditions. GroEL
1076 serves as a loading control. The red arrow indicates a low intensity disulfide-linked adduct
1077 band formed by GldK that is additional to the adduct with SprF. *, non-specific background
1078 band.

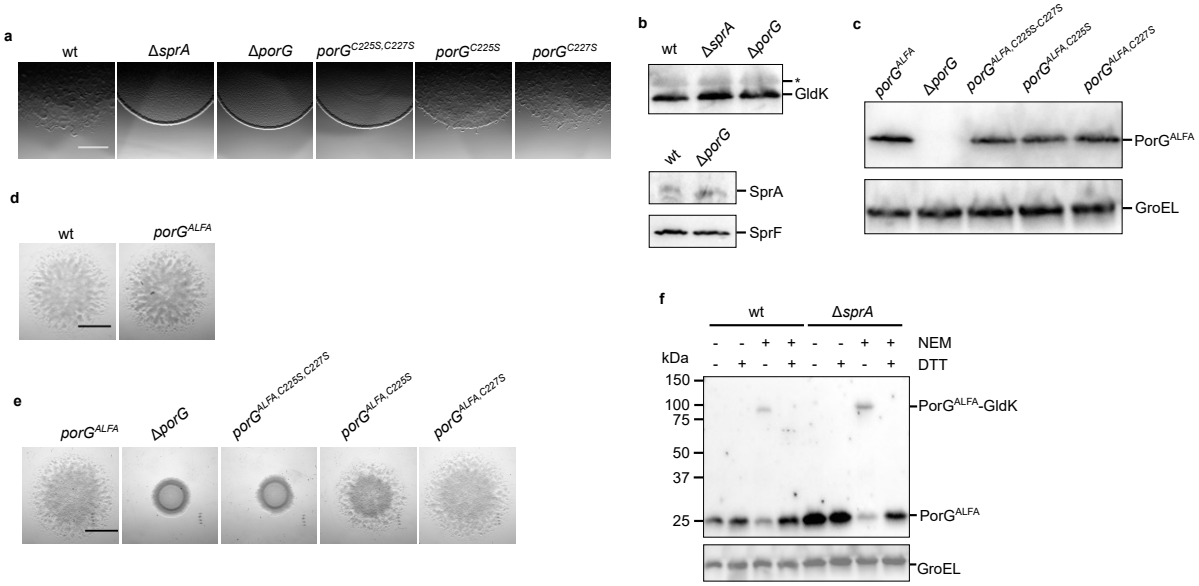

Extended Data Fig. 5 | Characterization of *F. johnsoniae* PorG.

a, Spreading (gliding) morphology of non-tagged PorG cysteine variants at 6 h. Scale bar, 1 mm.

b, *F. johnsoniae* PorG is not required for the expression and stability of the key T9SS and gliding components GldK, SprA, and SprF. Whole cell immunoblotting using antibodies against the indicated proteins. *, non-specific band.

c-e, Insertion of an ALFA-tag into loop 3 does not affect the stability or functionality of *F. johnsoniae* PorG and its variants.

c, Whole cells immunoblotting using ALFA-tag antibodies. GroEL serves as loading control.

d,e, Spreading (gliding) morphology on agar. Scale bar, 5mm.

f, Disulfide bond formation between PorG and GldK does not require T9SS activity. Strains with the indicated mutations were subject to whole cell immunoblotting with ALFA-tag antibodies. Where indicated the cells were pre-treated with NEM. At the SDS-PAGE step samples were run under either non-reducing (- DTT) or reducing (+ DTT) conditions. GroEL serves as a loading control. Δ*sprA*, strain missing the T9SS translocon.

a-f, Similar results were obtained from 3 biological repeats. wt, wild type.

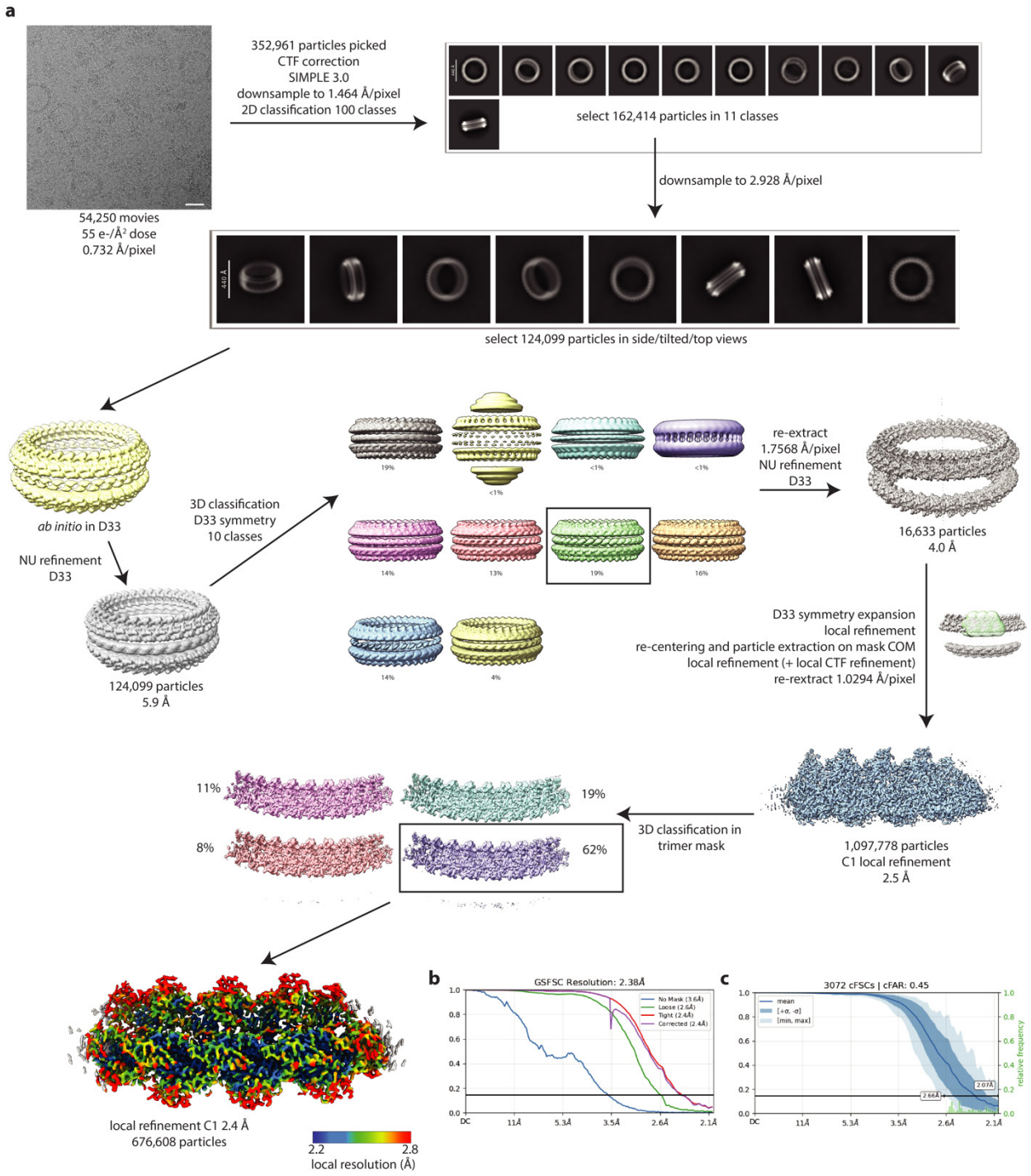

Extended Data Fig. 6 | Cryo-EM Workflow for the *P. gingivalis* PorKN complex structure. **a**, Image processing workflow, including the local resolution estimate of the volume. Micrograph scale bar is 300 Å.

b, Gold-standard Fourier Shell Correlation (FSC) curves used for global resolution estimation.

c, Conical FSC (cFSC) plot assessing directional signal content.

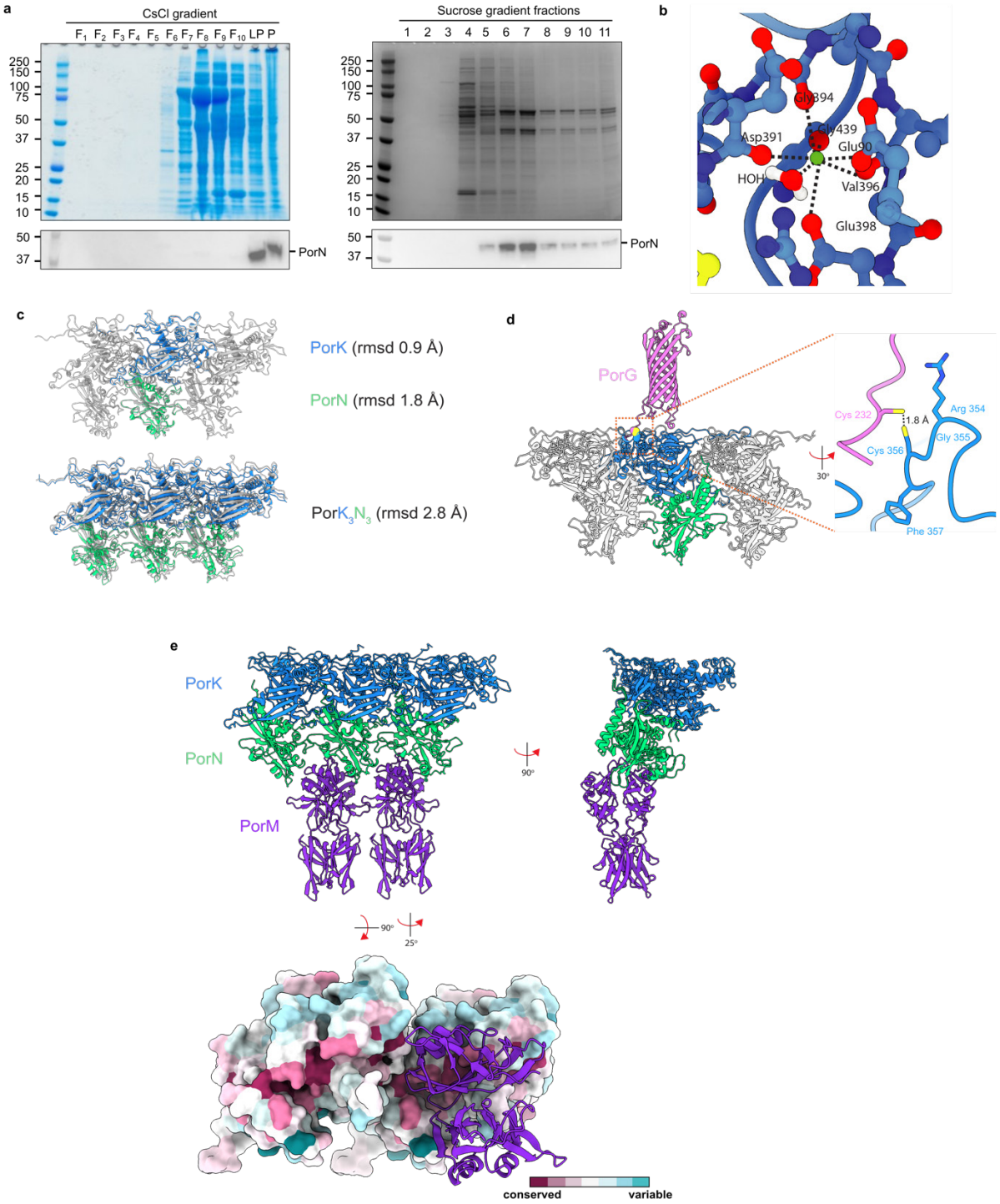

Extended Data Fig. 7 | Further information on the *P. gingivalis* PorKN complex.

a, Purification of the PorKN complex for structural analysis. The successive CsCl and sucrose density gradient steps of an exemplar preparation are shown. Coomassie Blue stained SDS-PAGE gels with corresponding anti-PorN immunoblots below. Fractions (F) are numbered from the tops of the gradients. P, pellet; LP, loose pellet. Fraction LP from the CsCl was loaded onto the sucrose gradient from which fractions F6 and F7 were pooled and used for structure determination.

b, The Ca^{2+} ion binding site in PorK with the metal ion (green) and co-ordinating ligands shown as atomic spheres.

c, AF3 reliably models the PorKN oligomer. AF3 models (coloured cartoons) of the isolated PorK and PorN subunits (Top) or of the complex between three PorKN units (Bottom) are superpositioned on a three PorKN unit section of the experimental structure (grey cartoons) with the indicated RMSDs.

d, AF3 model in cartoons representation for the complex formed between PorG and the PorKN ring. The model contains one copy of PorG and three copies of the PorKN unit. No protein-protein protein contacts are predicted beyond the intersubunit disulfide linkage.

e, AF3 model for the complex formed between the distal ends of the PorM motor arms and the PorKN ring. The model contains three copies of the PorKN unit and four copies of the D3-D4 fragment of PorM. Note that each PorM arm is a homodimer. (Top) Two views of the model in cartoons representation. (Bottom) The model viewed from the periplasm but with the PorKN units shown in spacefilling representation and coloured by sequence conservation using Consurf[66]. One of the PorM homodimer arms has been removed to allow the PorM interaction surface on PorKN to be inspected. The remaining PorM homodimer arm is shown in cartoons representation with the upper PorM subunit forming the potential specific interaction with PorKN.

References

1 Human Microbiome Project, C. Structure, function and diversity of the healthy human microbiome. Nature 486, 207-214 (2012). https://doi.org:10.1038/nature11234

2 Thomas, F., Hehemann, J. H., Rebuffet, E., Czjzek, M. & Michel, G. Environmental and gut bacteroidetes: the food connection. Front Microbiol 2, 93 (2011). https://doi.org:10.3389/fmicb.2011.00093

3 Veith, P. D., Glew, M. D., Gorasia, D. G. & Reynolds, E. C. Type IX secretion: the generation of bacterial cell surface coatings involved in virulence, gliding motility and the degradation of complex biopolymers. Mol Microbiol 106, 35-53 (2017). https://doi.org:10.1111/mmi.13752

4 Lasica, A. M., Ksiazek, M., Madej, M. & Potempa, J. The Type IX Secretion System (T9SS): Highlights and Recent Insights into Its Structure and Function. Front Cell Infect Microbiol 7, 215 (2017). https://doi.org:10.3389/fcimb.2017.00215

5 Veith, P. D., Glew, M. D., Gorasia, D. G., Cascales, E. & Reynolds, E. C. The Type IX Secretion System and Its Role in Bacterial Function and Pathogenesis. J Dent Res 101, 374-383 (2022). https://doi.org:10.1177/00220345211051599

6 Paillat, M., Lunar Silva, I., Cascales, E. & Doan, T. A journey with type IX secretion system effectors: selection, transport, processing and activities. Microbiology (Reading) 169 (2023). https://doi.org:10.1099/mic.0.001320

7 McBride, M. J. Bacteroidetes Gliding Motility and the Type IX Secretion System. Microbiol Spectr 7 (2019). https://doi.org:10.1128/microbiolspec.PSIB-0002-2018

8 Li, Y. et al. Identification of trypsin-degrading commensals in the large intestine. Nature 609, 582-589 (2022). https://doi.org:10.1038/s41586-022-05181-3

9 Buzun, E. et al. The Type 9 Secretion System enables sharing of fungal mannan by human gut Bacteroides. bioRxiv (2022). https://doi.org: https://doi.org/10.1101/2022.07.15.500217

10 Lauber, F., Deme, J. C., Lea, S. M. & Berks, B. C. Type 9 secretion system structures reveal a new protein transport mechanism. Nature 564, 77-82 (2018). https://doi.org:10.1038/s41586-018-0693-y

11 Lauber, F. et al. Structural insights into the mechanism of protein transport by the Type 9 Secretion System translocon. Nat Microbiol (2024). https://doi.org:10.1038/s41564-024-01644-7

12 Kulkarni, S. S., Zhu, Y., Brendel, C. J. & McBride, M. J. Diverse C-Terminal Sequences Involved in Flavobacterium johnsoniae Protein Secretion. J Bacteriol 199 (2017). https://doi.org:10.1128/JB.00884-16

13 Glew, M. D. et al. PorV is an Outer Membrane Shuttle Protein for the Type IX Secretion System. Sci Rep 7, 8790 (2017). https://doi.org:10.1038/s41598-017-09412-w

14 Kulkarni, S. S., Johnston, J. J., Zhu, Y., Hying, Z. T. & McBride, M. J. The Carboxy-Terminal Region of Flavobacterium johnsoniae SprB Facilitates Its Secretion by the Type IX Secretion System and Propulsion by the Gliding Motility Machinery. J Bacteriol 201 (2019). https://doi.org:10.1128/JB.00218-19

15 Gorasia, D. G. et al. Type B CTD Proteins Secreted by the Type IX Secretion System Associate with PorP-like Proteins for Cell Surface Anchorage. Int J Mol Sci 23 (2022). https://doi.org:10.3390/ijms23105681

16 Wadhwa, N. & Berg, H. C. Bacterial motility: machinery and mechanisms. Nat Rev Microbiol 20, 161-173 (2022). https://doi.org:10.1038/s41579-021-00626-4

17 Nelson, S. S., Bollampalli, S. & McBride, M. J. SprB is a cell surface component of the Flavobacterium johnsoniae gliding motility machinery. J Bacteriol 190, 2851-2857 (2008). https://doi.org:10.1128/JB.01904-07

18 Nakane, D., Sato, K., Wada, H., McBride, M. J. & Nakayama, K. Helical flow of surface protein required for bacterial gliding motility. Proc Natl Acad Sci U S A 110, 11145-11150 (2013). https://doi.org:10.1073/pnas.1219753110

19 Shibata, S. et al. Filamentous structures in the cell envelope are associated with bacteroidetes gliding machinery. Commun Biol 6, 94 (2023). https://doi.org:10.1038/s42003-023-04472-3

20 Miller, H., Kjaer, A., Coppola, S., Jones, R., Berks, B.C., and Berry, R.M. Architecture of the Bacteroidota gliding motility machinery revealed by 3D tracking of adhesin movements (2025).

21 Shrivastava, A., Roland, T. & Berg, H. C. The Screw-Like Movement of a Gliding Bacterium Is Powered by Spiral Motion of Cell-Surface Adhesins. Biophys J 111, 1008-1013 (2016). https://doi.org:10.1016/j.bpj.2016.07.043

22 Wada, H., Nakane, D. & Chen, H. Y. Bidirectional bacterial gliding motility powered by the collective transport of cell surface proteins. Phys Rev Lett 111, 248102 (2013). https://doi.org:10.1103/PhysRevLett.111.248102

23 Rhodes, R. G., Nelson, S. S., Pochiraju, S. & McBride, M. J. Flavobacterium johnsoniae sprB is part of an operon spanning the additional gliding motility genes sprC, sprD, and sprF. J Bacteriol 193, 599-610 (2011). https://doi.org:10.1128/JB.01203-10

24 Braun, T. F. & McBride, M. J. Flavobacterium johnsoniae GldJ is a lipoprotein that is required for gliding motility. J Bacteriol 187, 2628-2637 (2005). https://doi.org:10.1128/JB.187.8.2628-2637.2005

25 Shrivastava, A. & Berg, H. C. A molecular rack and pinion actuates a cell-surface adhesin and enables bacterial gliding motility. Sci Adv 6, eaay6616 (2020). https://doi.org:10.1126/sciadv.aay6616

26 Trivedi, A. M., J. A.; Henderson, E. C.; Singharoy, A.; Shrivastava, A. A membrane-associated conveyor belt controls the rotational direction of the bacterial type 9 secretion system. bioRxiv (2025). https://doi.org: https://doi.org/10.1101/2024.09.23.614571

27 Sato, K. et al. A protein secretion system linked to bacteroidete gliding motility and pathogenesis. Proc Natl Acad Sci U S A 107, 276-281 (2010). https://doi.org:10.1073/pnas.0912010107

28 Hennell James, R. et al. Structure and mechanism of the proton-driven motor that powers type 9 secretion and gliding motility. Nat Microbiol 6, 221-233 (2021). https://doi.org:10.1038/s41564-020-00823-6

29 Shrivastava, A., Johnston, J. J., van Baaren, J. M. & McBride, M. J. Flavobacterium johnsoniae GldK, GldL, GldM, and SprA are required for secretion of the cell surface gliding motility adhesins SprB and RemA. J Bacteriol 195, 3201-3212 (2013). https://doi.org:10.1128/JB.00333-13

30 Leone, P. et al. Type IX secretion system PorM and gliding machinery GldM form arches spanning the periplasmic space. Nat Commun 9, 429 (2018). https://doi.org:10.1038/s41467-017-02784-7

31 Rieu, M., Krutyholowa, R., Taylor, N. M. I. & Berry, R. M. A new class of biological ion-driven rotary molecular motors with 5:2 symmetry. Front Microbiol 13, 948383 (2022). https://doi.org:10.3389/fmicb.2022.948383

32 Gorasia, D. G. et al. Structural Insights into the PorK and PorN Components of the Porphyromonas gingivalis Type IX Secretion System. PLoS Pathog 12, e1005820 (2016). https://doi.org:10.1371/journal.ppat.1005820

1229 33 Song, L. et al. A unique bacterial secretion machinery with multiple secretion centers.
1230 Proc Natl Acad Sci U S A 119, e2119907119 (2022).
1231 https://doi.org:10.1073/pnas.2119907119

1232 34 Gorasia, D. G. C., G.; Seers, C.A.; Butler, C.A.; Heath, J.E.; Glew, M.D.; McBride,
1233 M.J.; Subramanian, P.; Kjær, A.; Jensen, G.J.; Veith, P.D.; Reynolds, E.C. In situ
1234 structure and organisation of the type IX secretion system. bioRxiv (2020).

1235 35 Braun, T. F., Khubbar, M. K., Saffarini, D. A. & McBride, M. J. Flavobacterium
1236 johnsoniae gliding motility genes identified by mariner mutagenesis. J Bacteriol 187,
1237 6943-6952 (2005). https://doi.org:10.1128/JB.187.20.6943-6952.2005

1238 36 Abramson, J. et al. Accurate structure prediction of biomolecular interactions with
1239 AlphaFold 3. Nature 630, 493-500 (2024). https://doi.org:10.1038/s41586-024-07487-
1240 w

1241 37 Kjaer, A. Investigating bacteroidetes gliding motility, University of Oxford, (2022).

1242 38 Naito, M., Tominaga, T., Shoji, M. & Nakayama, K. PGN_0297 is an essential
1243 component of the type IX secretion system (T9SS) in Porphyromonas gingivalis: Tn-
1244 seq analysis for exhaustive identification of T9SS-related genes. Microbiol Immunol
1245 63, 11-20 (2019). https://doi.org:10.1111/1348-0421.12665

1246 39 Ono, S. et al. Construction and Characterization of a PGN_0297 Mutant of
1247 Porphyromonas gingivalis: Evidence of the Contribution of PGN_0297 to Gingipain
1248 Activity. Acta Med Okayama 73, 315-323 (2019). https://doi.org:10.18926/AMO/56933

1249 40 Nakayama, K. Porphyromonas gingivalis and related bacteria: from colonial
1250 pigmentation to the type IX secretion system and gliding motility. J Periodontal Res 50,
1251 1-8 (2015). https://doi.org:10.1111/jre.12255

1252 41 Johnson, S. et al. Molecular structure of the intact bacterial flagellar basal body. Nat
1253 Microbiol 6, 712-721 (2021). https://doi.org:10.1038/s41564-021-00895-y

1254 42 Johnson, S. et al. Structural basis of directional switching by the bacterial flagellum.
1255 Nat Microbiol 9, 1282-1292 (2024). https://doi.org:10.1038/s41564-024-01630-z

1256 43 Dierks, T. et al. Molecular basis for multiple sulfatase deficiency and mechanism for
1257 formylglycine generation of the human formylglycine-generating enzyme. Cell 121,
1258 541-552 (2005). https://doi.org:10.1016/j.cell.2005.03.001

1259 44 Fuchsbauer, O., Lunar Silva, I., Cascales, E., Roussel, A. & Leone, P. Structural and
1260 functional analyses of the Porphyromonas gingivalis type IX secretion system PorN
1261 protein. J Biol Chem 298, 101618 (2022). https://doi.org:10.1016/j.jbc.2022.101618

1262 45 Vincent, M. S. et al. Dynamic proton-dependent motors power type IX secretion and
1263 gliding motility in Flavobacterium. PLoS Biol 20, e3001443 (2022).
1264 https://doi.org:10.1371/journal.pbio.3001443

1265 46 Vincent, M. S. et al. Characterization of the Porphyromonas gingivalis Type IX
1266 Secretion Trans-envelope PorKLMNP Core Complex. J Biol Chem 292, 3252-3261
1267 (2017). https://doi.org:10.1074/jbc.M116.765081

1268 47 Johnston, J. J., Shrivastava, A. & McBride, M. J. Untangling Flavobacterium
1269 johnsoniae Gliding Motility and Protein Secretion. J Bacteriol 200 (2018).
1270 https://doi.org:10.1128/JB.00362-17

1271 48 Kadokura, H. & Beckwith, J. Detecting folding intermediates of a protein as it passes
1272 through the bacterial translocation channel. Cell 138, 1164-1173 (2009).
1273 https://doi.org:10.1016/j.cell.2009.07.030

1274 49 Landeta, C., Boyd, D. & Beckwith, J. Disulfide bond formation in prokaryotes. Nat
1275 Microbiol 3, 270-280 (2018). https://doi.org:10.1038/s41564-017-0106-2

1276 50 Worrall, L. J., Majewski, D. D. & Strynadka, N. C. J. Structural Insights into Type III
1277 Secretion Systems of the Bacterial Flagellum and Injectisome. Annual review of
1278 microbiology 77, 669-698 (2023). https://doi.org:10.1146/annurev-micro-032521-
1279 025503

1280 51 McBride, M. J. & Kempf, M. J. Development of techniques for the genetic manipulation
1281 of the gliding bacterium Cytophaga johnsonae. J Bacteriol 178, 583-590 (1996).

1282 52 Liu, J., McBride, M. J. & Subramaniam, S. Cell surface filaments of the gliding
1283 bacterium Flavobacterium johnsoniae revealed by cryo-electron tomography. J
1284 Bacteriol 189, 7503-7506 (2007). https://doi.org:10.1128/JB.00957-07

1285 53 Agarwal, S., Hunnicutt, D. W. & McBride, M. J. Cloning and characterization of the
1286 Flavobacterium johnsoniae (Cytophaga johnsonae) gliding motility gene, gldA. Proc
1287 Natl Acad Sci U S A 94, 12139-12144 (1997).

1288 54 Gibson, D. G. et al. Enzymatic assembly of DNA molecules up to several hundred
1289 kilobases. Nat Methods 6, 343-345 (2009). https://doi.org:10.1038/nmeth.1318

1290 55 Zhu, Y. et al. Genetic analyses unravel the crucial role of a horizontally acquired
1291 alginate lyase for brown algal biomass degradation by Zobellia galactanivorans.
1292 Environ Microbiol 19, 2164-2181 (2017). https://doi.org:10.1111/1462-2920.13699

56 Stafford, P. et al. Gingipain-dependent degradation of mammalian target of rapamycin pathway proteins by the periodontal pathogen Porphyromonas gingivalis during invasion. Mol Oral Microbiol 28, 366-378 (2013). https://doi.org:10.1111/omi.12030

57 Nelson, S. S., Glocka, P. P., Agarwal, S., Grimm, D. P. & McBride, M. J. Flavobacterium johnsoniae SprA is a cell surface protein involved in gliding motility. J Bacteriol 189, 7145-7150 (2007). https://doi.org:10.1128/JB.00892-07

58 Ovesny, M., Krizek, P., Borkovec, J., Svindrych, Z. & Hagen, G. M. ThunderSTORM: a comprehensive ImageJ plug-in for PALM and STORM data analysis and super-resolution imaging. Bioinformatics 30, 2389-2390 (2014). https://doi.org:10.1093/bioinformatics/btu202

59 Gorasia, D. G., Hanssen, E., Veith, P. D. & Reynolds, E. C. Structural Characterization of the Type IX Secretion System in Porphyromonas gingivalis. Methods Mol Biol 2210, 113-121 (2021). https://doi.org:10.1007/978-1-0716-0939-2_11

60 Caesar, J. et al. SIMPLE 3.0. Stream single-particle cryo-EM analysis in real time. J Struct Biol X 4, 100040 (2020). https://doi.org:10.1016/j.yjsbx.2020.100040

61 Punjani, A., Zhang, H. & Fleet, D. J. Non-uniform refinement: adaptive regularization improves single-particle cryo-EM reconstruction. Nat Methods 17, 1214-1221 (2020). https://doi.org:10.1038/s41592-020-00990-8

62 Brown, A. et al. Tools for macromolecular model building and refinement into electron cryo-microscopy reconstructions. Acta Crystallogr D Biol Crystallogr 71, 136-153 (2015). https://doi.org:10.1107/S1399004714021683

63 Afonine, P. V. et al. Real-space refinement in PHENIX for cryo-EM and crystallography. Acta Crystallogr D Struct Biol 74, 531-544 (2018). https://doi.org:10.1107/S2059798318006551

64 Williams, C. J. et al. MolProbity: More and better reference data for improved all-atom structure validation. Protein Sci 27, 293-315 (2018). https://doi.org:10.1002/pro.3330

65 Pettersen, E. F. et al. UCSF ChimeraX: Structure visualization for researchers, educators, and developers. Protein Sci 30, 70-82 (2021). https://doi.org:10.1002/pro.3943

66 Ashkenazy, H. et al. ConSurf 2016: an improved methodology to estimate and visualize evolutionary conservation in macromolecules. Nucleic Acids Res 44, W344-350 (2016). https://doi.org:10.1093/nar/gkw408